Factors controlling pore network development of thermally mature Early Palaeozoic mudstones from the Baltic Basin (N Poland)

Słomski, P.; Szczepański, J.; Topór, T.; Mastalerz, M.; Pluymakers, A.; Derkowski, A.; Wojciechowski, T.

DOI
10.1016/j.marpetgeo.2021.105328

Publication date
2021

Document Version
Final published version

Published in
Marine and Petroleum Geology

Marine and Petroleum Geology 134 (2021) 105328

Contents lists available at ScienceDirect

Marine and Petroleum Geology

journal homepage: www.elsevier.com/locate/marpetgeo

Factors controlling pore network development of thermally mature Early Palaeozoic mudstones from the Baltic Basin (N Poland)

P. Słomski [a,*,1], J. Szczepański [b], T. Topór [c,2], M. Mastalerz [d], A. Pluymakers [e,3], A. Derkowski [f], T. Wojciechowski [g]

[a] Polish Geological Institute-National Research Institute, Rakowiecka 4, Warsaw, 00-975, Poland
[b] Institute of Geological Sciences, University of Wrocław, Plac Maksa Borna 9, Wrocław, 50-204, Poland
[c] Oil and Gas Institute – National Research Institute, Lubicz 25A, 31-503, Krakow, Poland
[d] Indiana Geological and Water Survey, Indiana University, 1001 E 10th Street, Bloomington, IN, 47405, United States
[e] Faculty of Civil Engineering and Geosciences, Technical University Delft, Stevinweg 1 / PO-box 5048 2628 CN Delft / 2600 GA, Delft, the Netherlands
[f] Institute of Geological Sciences, Polish Academy of Sciences, Research Centre in Krakow, Senacka St. No. 1, PL-31002, Krakow, Poland
[g] Institute of Physics, Polish Academy of Sciences, Lotników 32/46, 02-668, Warsaw, Poland

ARTICLE INFO

Keywords:
Shales
Baltic basin
Petrography and mineralogy
Types of porosity
Pore network development

ABSTRACT

Understanding the formation of pore space, especially in low porosity shales (as source rocks and as unconventional resources), is critical to the oil and gas industry, since pores control the space available for hydrocarbon and participate in hydrocarbon transport. We examined 87 Ordovician and Silurian mudstone samples collected from four wells located in the Pomeranian part of the Baltic Basin (northern Poland), one of the primary Polish targets for hydrocarbon exploration. These samples represent the Pelplin, the Pasłęk, the Jantar, the Prabuty, and the Sasino Formations, which still requires more detailed porosity studies. Our study aimed to identify factors controlling porosity development, by applying bulk techniques (organic petrology and TOC analyses, quantitative mineralogy, and porosimetry) as well as nano-to microscale techniques (thin section petrography, electron microscopy). The studied samples are mainly argillaceous mudstones. The results of porosimetry measurements, combined with image analysis, indicate that the pores of all studied rocks are dominated by micropores (pores <2 nm in diameter), mesopores (2–50 nm in diameter) and small macropores. The SEM images showed three main pore types: a) voids related to clay mineral aggregates, b) pores inside organic matter particles, and c) pores between other mineral grains. In the Jantar and Sasino mudstones, the organic matter content and its thermal maturity control porosity. The occurrence of solid bitumen in the rocks from these formations reduces samples' mesoporosity because of the pore-clogging effect. In contrast, in the Pasłęk and Prabuty Formations, there is low organic matter content and specific surface area and the volume of mesopores increase with clay minerals content. In the Pelplin mudstones, there are no prevailing factors controlling porosity. Finally, we suggest that a combination of SEM image analysis and dual liquid porosity (DLP) measurements is a powerful method to assess porosity available for petroleum flow in mudstones.

1. Introduction

During the last decade, interest in the exploration and extraction of hydrocarbons from unconventional reservoirs has grown (Middleton et al., 2017; Wang, 2018; Wang and Krupnick, 2013), with a particular focus on shale gas exploration (Cooper et al., 2016). This interest stimulated a wide range of studies dedicated to understanding mineralogical, petrophysical, and geochemical properties of fine-grained sedimentary rocks (Bu et al., 2015; Hackley and Cardott, 2016; Mastalerz et al., 2013; Nuttal et al., 2005; Topór et al., 2017a). An unconventional mudstone play commonly comprises a sedimentary succession dominated by nanoDarcy- and submicroDarcy-scale permeability rocks

* Corresponding author.
E-mail address: pslo@pgi.gov.pl (P. Słomski).
[1] Formerly with Institute of Geological Sciences, University of Wrocław.
[2] Formerly with Institute of Geological Sciences, Polish Academy of Sciences.
[3] Formerly with Physics of Geological Processes, University of Oslo, P.O. 1048, Blindern, 0316, Oslo, Norway.

https://doi.org/10.1016/j.marpetgeo.2021.105328
Received 5 December 2020; Received in revised form 5 September 2021; Accepted 8 September 2021
Available online 13 September 2021

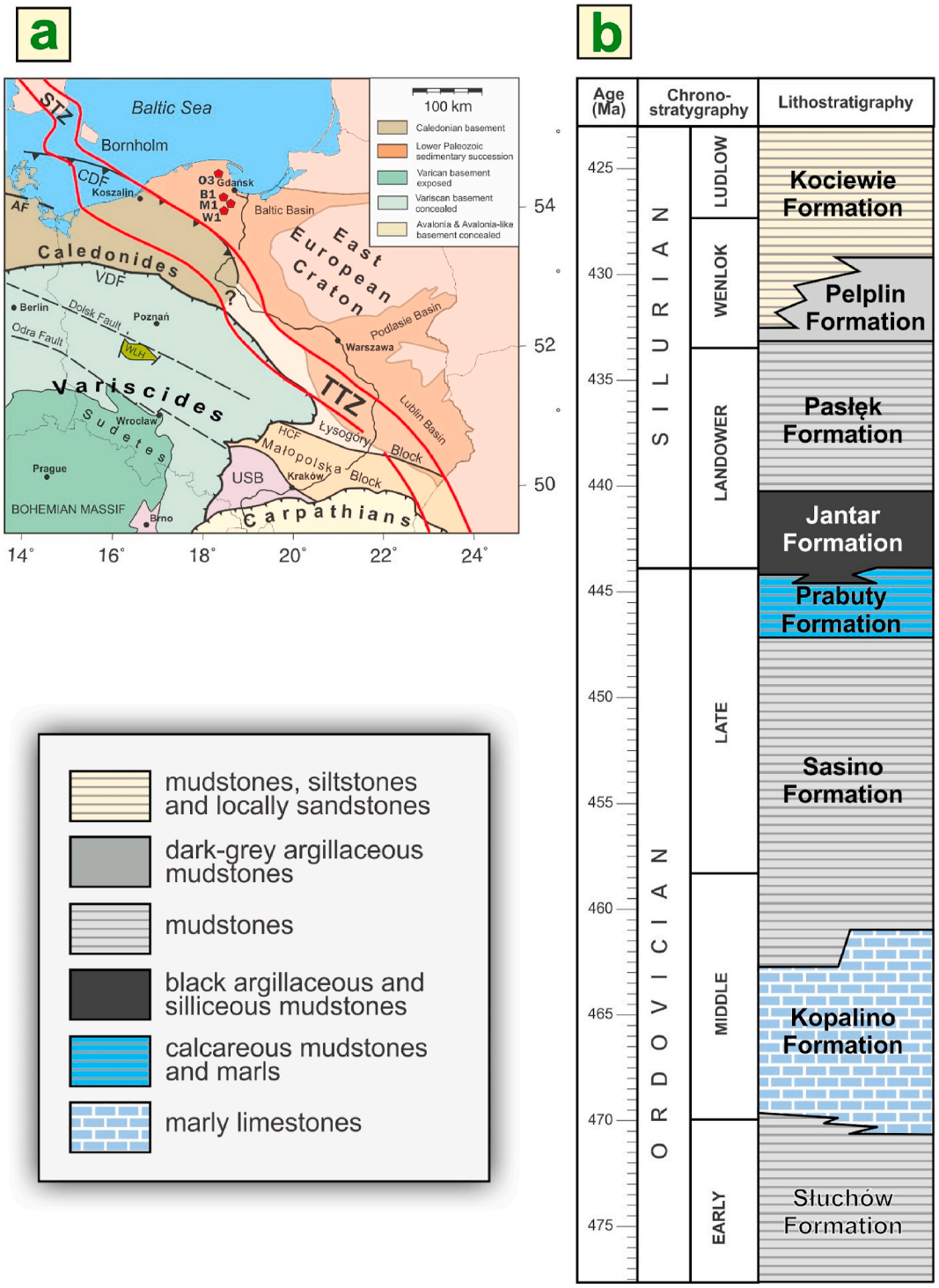

Fig. 1. Location of the studied boreholes O3, B1, M1, and W1 in the Baltic Basin. Map of Early Palaeozoic basins at the SW margin of East European Craton and the main pre-Permian tectonic units of Poland after Mazur et al., 2018 CDF = Caledonian deformation front, STZ = Sorgenfrei-Teisseyre Zone, TTZ = Teisseyre-Tornquist Zone, USB = Upper Silesia Block, VDF = Variscan deformation front, WLH = Wolsztyn-Leszno High, HCF = Holy Cross Fault. The Polish Oil and Gas Company requires keeping the name of these boreholes encoded and only allows schematic indication of their locations.

of clay-to silt-fraction, respectively. The main mineral constituents are rigid components such as quartz, calcite, or feldspar, whereas the elastic components are various clay minerals and organic matter (OM). Pore spaces developed within and along the abovementioned components can be filled with formation water, hydrocarbons, or other gases (Dayal, 2017). Therefore, for the purpose of estimating the potential of unconventional hydrocarbon resources, a multidisciplinary approach involving the characterization of mineral composition, OM, and porosity is necessary (Jiang et al., 2016; Ross and Marc Bustin, 2009).

The Early Palaeozoic successions in the Polish part of the Baltic Basin were and still are regarded as an important potential source and reservoir plays (*Shale gas in Poland-prospecting and exploration: 2007-2016 as of 29 February 2016, 2016*, Podhalańska et al., 2020). Several studies were devoted to the characterization of these rocks in terms of their mineralogical composition, OM content, thermal maturity, porosity, and permeability (Karnkowski, 2007; Kiersnowski and Dyrka, 2013; Kuila

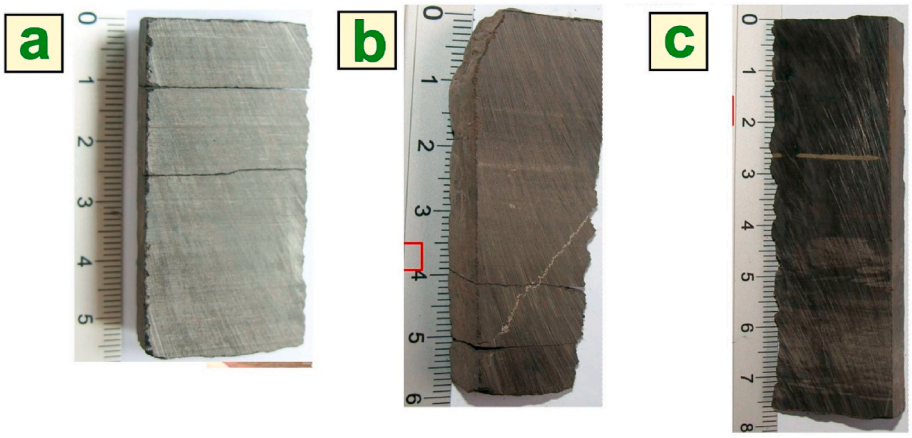

Fig. 2. Photographs of analysed mudstone samples from (a) the Pelplin Formation, (b) the Jantar Formation, and (c) the Sasino Formation. The lamination and colour of these rocks stem mainly from various amounts of organic matter, as well as the proportion of quartz and clay minerals. (For interpretation of the references to colour in this figure legend, the reader is referred to the Web version of this article.)

et al., 2014a; Milliken et al., 2018; Poprawa, 2010; Porębski et al., 2013; Topór et al., 2017a, 2017b). While the previous studies were of more regional nature, in this study we focused on a relatively small depth interval of ca. 100 m in four wells, which enabled us to track subtle differences in the samples. To date, few studies (on Late Palaeozoic rocks from the Baltic Basin) exist that use both a large number of samples as well as such a wide array of methods. We used a combination of analytical methods covering the mineral and petrographic description, image analysis for pore typing, geochemistry, organic petrology, and porosimetry of the mudstone samples. The level of details obtained in this study provides new insights into the pore types, porosity distribution, and defines the main factors controlling porosity in each lithostratigraphic unit of these Ordovician and Silurian mudstones. Moreover, we suggest that a combination of dual liquid porosimetry (DLP) and analysis of scanning electron microscopy (SEM) images can enable estimation of the porosity values range, where the flow of petroleum is possible.

2. Geological background

The Baltic Basin is one of three Lower Palaeozoic basins located at the western slope of the East European Craton (Fig. 1a). The formation of the Baltic Basin occurred in several stages (Mazur et al., 2018; Poprawa, 2010; Poprawa et al., 1999). The first stage was associated with rifting along the southwest margin of Baltica from the late Vendian to the middle Cambrian. Later, the formation of the basin was controlled by the thermal subsidence of the Baltica margin from the middle Cambrian to the Middle Ordovician. Finally, the subsidence continued in response to flexural bending during the Caledonian collision in the late Ordovician and Silurian (Mazur et al., 2018; Porębski et al., 2013). The Ordovician to Silurian sediments in the Baltic Basin are dominated by dark graptolite-rich shales, marly limestones, siltstones, and, locally, sandstones (Poprawa, 2010; Porębski et al., 2013). This sequence is currently buried at depths of ca. 1500–4000 m (Poprawa, 2010), while its thickness varies from 0 to ca. 4000 m (Porębski and Podhalańska, 2019). The amount of total organic carbon (TOC) in the Early Palaeozoic deposits from the Baltic Basin ranges from 0 to ca. 12% (Poprawa, 2010). The thermal maturity level of OM in the Ordovician and Silurian mudstones in the whole Baltic Basin, expressed by vitrinite reflectance equivalent (VRE), has a wide range from ca. 0.4–4.9% (Grotek, 2006).

3. Samples and methods

Eighty-seven mudstone samples were collected from four wells (O3, W1, M1, and B1) drilled by the Polish Oil and Gas Company. The wells are located in the Pomeranian part of the Baltic Basin (Fig. 1a). The investigated samples cover the Ordovician Sasino and Prabuty Formations and Silurian Pasłęk, Jantar, and Pelplin Formations (Fig. 1b). The examined stratigraphic interval comprises grey and dark grey, mostly argillaceous, mudstones (Fig. 1b).

Our study is based on a combination of several techniques, namely thin section petrography, organic petrology and TOC analyses, electron microscopy imaging, quantitative mineralogy, and porosimetry measurements. However, owing to the limited amount of rock material, not all types of analyses were performed on the whole suite of 87 samples (Fig. A1, in Appendix A). The petrographic description of thin sections was performed for 40 samples, using a Nikon ECLIPS LV100 POL microscope. The samples have been chosen to represent each lithostratigraphic unit (between 4 thin sections from the Pelplin Formation and 16 thin sections from the Sasino Formation). The maceral composition of the OM and the relative abundance of macerals were assessed visually on pellets prepared from 70 samples, using a Leica DM 2500 P microscope, both in white and fluorescent light mode under oil immersion. The pellets were prepared from samples crushed to ~ 1 mm and polished mechanically using a Leco GPX 200 polisher, taking special care for consistent and repeatable sample treatment. In the absence of vitrinite, the reflectance of solid bitumen (SBR_o) was measured to evaluate thermal maturity on 68 samples. For each sample, 25 measurements of different solid bitumen particles were collected and the microscope was calibrated using a glass standard of 1.01% reflectance. The precision of the instrument was equal or less than 0.01%. Results were recalculated to the VRE scale using the equation provided by Jacob (1989). For 85 samples, TOC concentrations were measured at Acme Labs using a LECO apparatus.

To determine the mineral composition, 79 powdered specimens were prepared for X-ray diffraction analyses (XRD). The XRD measurements were carried out at the Institute of Geological Sciences–Polish Academy of Sciences (IGS-PAS). Samples were first crushed in a mortar to fraction <0.43 mm and then homogenized in a laboratory splitter; portions were ground with methanol in a McCrone Micronizing Mill with the addition of 10 wt % ZnO as an internal standard. Grinding was performed for 5 min to obtain particles smaller than 20 μm. Prepared samples were loaded into side-loaded holders. Powder X-ray diffractograms were recorded between 5 and 65° 2Θ using CuKα radiation and counting time 2s/0.02° 2Θ step. The obtained diffractograms were analysed using the in-house Q-Min software (by Dr. Hab. M. Szczerba, IGS-PAS). Theoretical details of this method are given in Środoń (2001).

For nine samples representing four formations, scanning electron microscopy (SEM) images were obtained in backscatter electron mode (SEM BSE) using a FEI Helios NanoLab microscope at the former

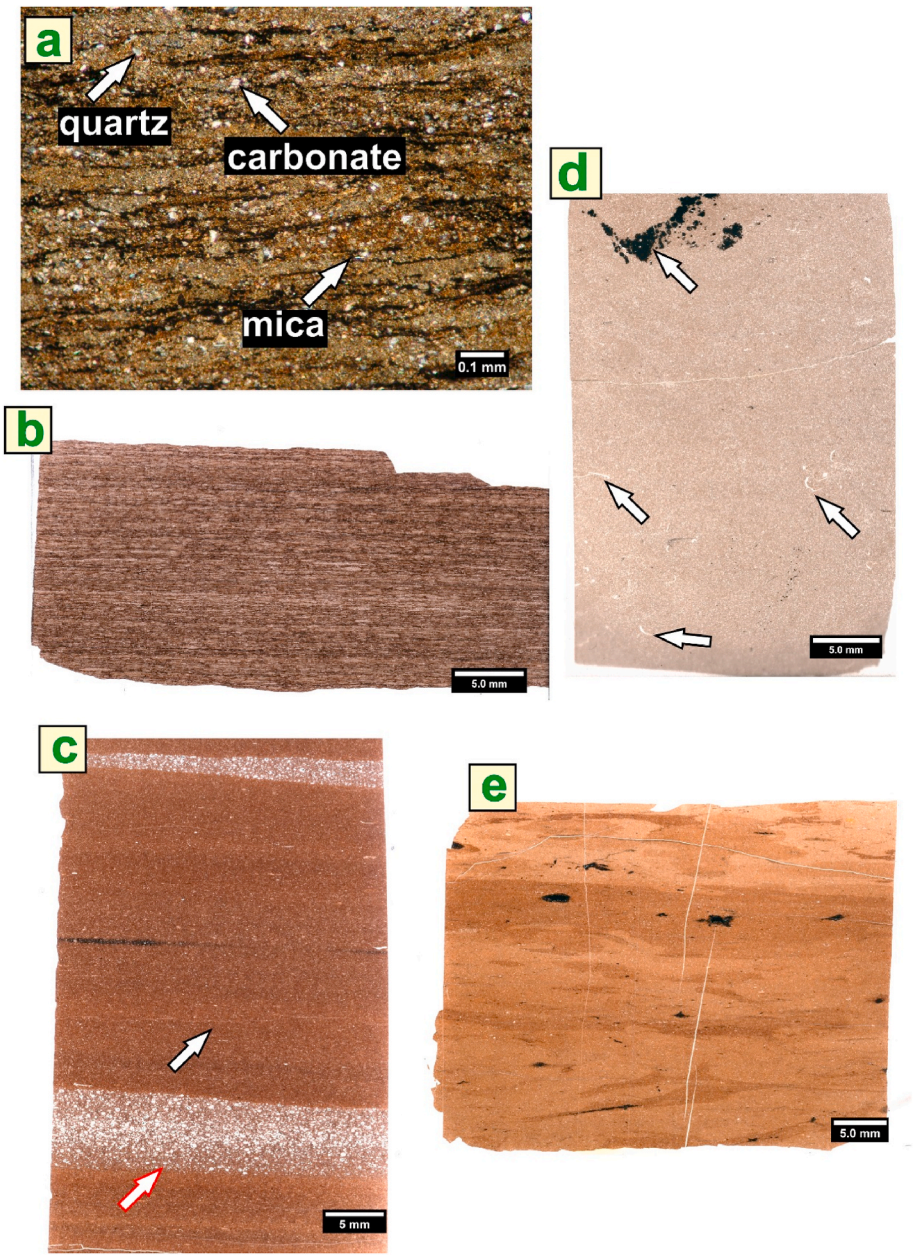

Fig. 3. (a) The described mudstones are usually matrix-supported, with framework grains of quartz, mica, and carbonates. The diameter of quartz and carbonate grains varies from 25 to 50 μm, while the length of mica flakes is up to 100 μm. Opaque minerals are mainly pyrite. Four structural types designated by their dominant sedimentary structure appear among studied samples: (b) Wavy, parallel, and continuous lamination is often defined by the presence of lens-shaped intraclasts. This type of lamination is prevalent in mudstones from the Pelplin Formation. (c) Planar, parallel, and continuous lamination is underlined by various laminae widths and colours (marked by arrows). In some samples, we found relatively thick (up to ca. 500 μm) lamina enriched in quartz (red arrow). (d) Homogenous mudstone containing large irregular concretion of pyrite (marked by arrow) and shell detritus (marked by arrows), (e) Highly bioturbated mudstones, which are especially common in the Sasino Formation. (For interpretation of the references to colour in this figure legend, the reader is referred to the Web version of this article.)

Wrocław Research Centre EIT+ (currently Łukasiewicz Research Network–PORT Polish Centre for Technology Development). The main criterion for selecting the samples was to analyse at least one sample representing each of the sedimentary structure type as described during thin section inspection. Samples were polished, then ion milled and coated with graphite before the imaging process. Ion milling was performed in Leica EM TIC 3x equipment, with 6° tilt angle and 200–300 μA current. The polished area of in case of each sample was in the range of ca. 0.5–1 cm^2. Because the thermal maturity of studied samples is slightly higher than 1% in the VRE scale, we assume that ion milling did not severely affect the maturity and porosity of OM fragments (Mastalerz and Schieber, 2017; Schieber et al., 2016). For each of these nine samples, large high-resolution SEM BSE maps were created using between 64 and 200 single images, 5 nm/pixel resolution. Image processing was performed in the open-source software Fiji (Schindelin et al., 2012). Common Fiji built-in functions were used to improve the quality of images, while the Grid Collection Stitching plugin (Preibisch et al., 2009) enabled merging the single images into large SEM BSE maps, with the surface area ranging from 3600 to 11 000 μm^2 for a particular sample. Such an area of analysed samples represents the same order of magnitude as in works dedicated to image analysis of fine-grained rocks (e.g., Hemes et al., 2015; Houben et al., 2013).

Furthermore, seven out of nine samples were analysed with a SEM coupled with a focused ion beam (FIB-SEM). Six of these samples were analysed using the FEI Helios NanoLab instrument. Additionally, one sample was analysed using Carl Zeiss Crossbeam Auriga microscope at the Institute of Physics–Polish Academy of Science (IF PAN) in Warsaw. For all inspected samples, we performed FIB-SEM imaging in the regions where the porosity was clearly visible in SEM-BSE images. The imaging process was carried out in BSE mode, with the resolution of a single 2-D image around 7–9 nm/pixel. Before FIB-SEM imaging, the selected area of each samples' surface was coated with platinum to enable the precise cutting of each slice of the rock. The samples were already coated by graphite layer after the SEM BSE imaging, however additionally, a silver paste was used to prevent charging. Obtained 2-D images were aligned in the Fiji software by the usage of the *Register Virtual Stack Slices* plugin.

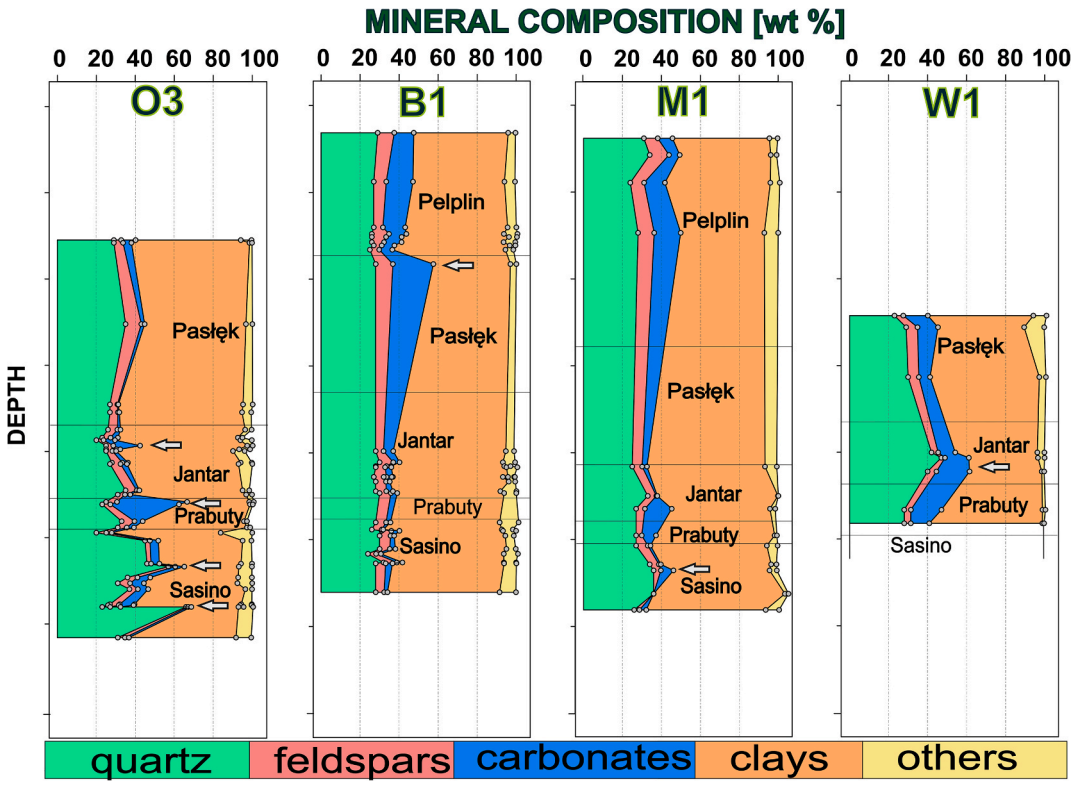

Fig. 4. Vertical variations of mineralogical composition in O3, B1, M1, and W1 wells. The diagrams show amounts of quartz, feldspars (alkaline and potassium feldspars), carbonates (calcite, ankerite and dolomite), and clay minerals (illite, muscovite, smectite, illite-smectite mixed layers phases, as well as kaolinite and chlorites). The remaining minerals—pyrite, barite, gypsum, apatite, iron (oxy)hydroxide, and rutile—are shown together. Arrows marked samples having an increased amount of quartz or carbonates.

Between 150 and 300 images were collected and aligned for each sample, with a step ca. 10–15 nm and with an area of up to ca. 60 μm^2. This results in voxel volumes ranging from 500 to 1200 nm^3, and the total volume of the analysed cuboid reaches up to 150 μm^3. For processing and visualization of FIB-SEM data, we mainly used the Fiji software. However, for sample SQ632.21, we used Avizo© software. During both SEM and FIB-SEM analysis, the mineralogical composition of the inspected samples was controlled using energy-dispersive X-ray spectroscopy (EDS).

Based on the obtained SEM BSE and FIB-SEM images, the total visible porosity was calculated. We applied automatic segmentation of porosity from the original images and created binary images of porosity, which were manually inspected for the exclusion of mistakenly segmented pores. The pore size distribution (PSD) in SEM BSE images was determined, by the procedure of fitting an ellipse to every single pore separated in SEM BSE. The shorter axis of each fitted ellipse was taken as an equivalent pore diameter. These analyses were conducted in Fiji software by applying the built-in Analyse Particles plugin. A detailed description of image processing and analysis steps, as well as an example of porosity segmentation procedure, is provided in Appendix B. PSD data based on the SEM BSE images were analysed and presented as empirical distribuant functions (ECDF) and kernel density estimator curves (KDE), which were done in the R environment by *ecdf* and *density* functions, respectively, from the stats package (R Core Team, 2020). Since the SEM BSE images resolution equals 5 nm/pixel and the FIB-SEM single image (two-dimensional) resolution equals 7–9 nm/pixel, we assumed a "conservative" estimate of the detection limit of the minimal equivalent pore diameter to be 10 nm.

Low-pressure nitrogen (N_2) and carbon dioxide (CO_2) adsorption measurements were performed for 75 samples at Indiana University's Indiana Geological and Water Survey in Bloomington using a Micromeritics ASAP 2020 apparatus. Shale aliquots weighing from 1.5 to 2 g, crushed and sieved with a size 200 mesh (75 μm) were degassed for approximately 18 h at the temperature of 383.15 K and pressure <10 μm Hg. While CO2 measurements were run at 273.15 K, N2 measurements were performed at 77 K. The relative pressure P/P_0 (where P is the actual gas pressure and P_0 is the vapour pressure of the adsorbing gas) range was from 0.075 to 0.995 (for N_2 adsorption), and from 0 to 0.03 (for CO_2 adsorption). The chosen particle size of analysed powders (75 μm) was assumed to be most appropriate for gas adsorption techniques in shale analysis (Mastalerz et al., 2017).

Analysis with N2 adsorption delivered information concerning mesopores (2–50 nm diameter) and also on the macropores <200 nm, whereas CO2 adsorption analysis supplied information concerning micropores (<2 nm diameter). The classification of porosity used in this study is based on the guidelines of the International Union of Pure and Applied Chemistry (Rouquerol et al., 1994), which distinguishes micropores (<2 nm), mesopores (2–50 nm), and macropores (>50 nm). The porosity of investigated samples was described using the following parameters:

(1) the specific surface area of pores (based on Brunauer-Emmet-Teller model, S_{BET}),
(2) the specific volume of mesopores (based on the Barret-Joyner-Halenda model, V_{BJH}),
(3) the specific volume of micropores (Dubinin–Astakhov model, V_{DA}).

The dual liquid porosimetry technique (DLP) was applied to obtain porosity of the studied samples (Kuila et al., 2014a; Topór et al., 2016). The DLP method covers two techniques: water immersion porosity (WIP) and kerosene immersion porosity (KIP), in which deionised water and light kerosene are used as immersion fluids, respectively. In both cases, the porosity calculations are based on measurements of grain

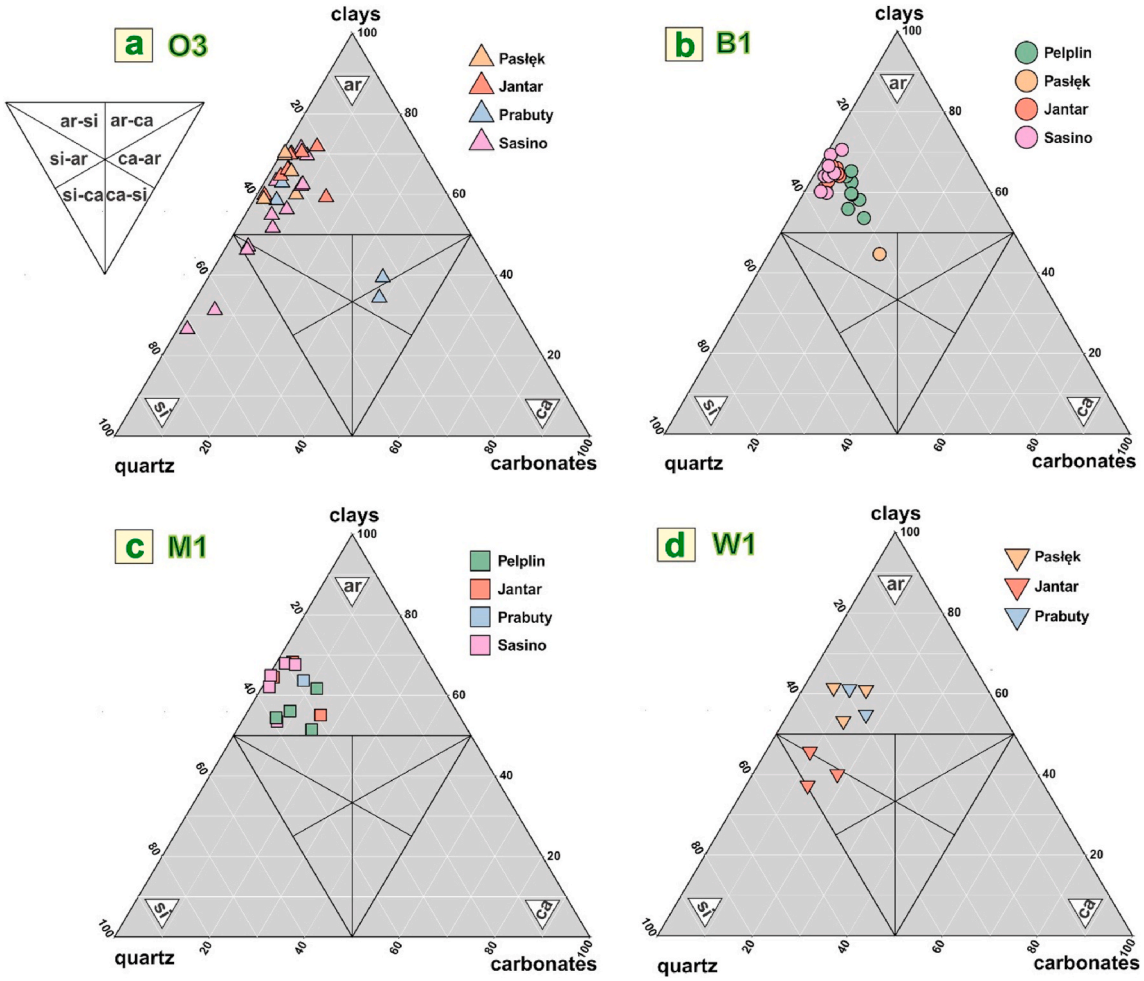

Fig. 5. The main mineral components (quartz, carbonates, and clay minerals) of examined samples are shown on separate ternary diagrams for clarity. (a) Mudstones from O3 well, (b) mudstones from B1 well, (c) mudstones from M1 well, (d) mudstone from W1 well. Nomenclature and abbreviations (ar = argillaceous, si = siliceous, ca = calcareous) after Lazar et al. (2015).

density and bulk density of rocks, which are obtained in accordance with Archimedes' law (Kuila et al., 2014a; Topór et al., 2016). The same rock chip was analysed with WIP and KIP for 68 samples. The WIP technique enables the calculation of total water accessible porosity ($Ø_{WIP}$), including the spaces occupied by water strongly adsorbed on the surface of clay minerals (clay-bound water). The KIP measurements allow the calculation of the total porosity accessible for liquid hydrocarbons ($Ø_{KIP}$). Usually, in a water-sensitive rock such as shale, the WIP values will be higher than the KIP.

4. Results

4.1. Petrography and mineralogical composition

The investigated samples are finely laminated mudstones, having laminae widths varying from less than 1 mm up to few millimetres (Fig. 2). Lamination predominantly results from variations in mineral composition (clay-rich versus more silty material) and the presence of dispersed OM (Fig. 2). The concentration of OM also affects sample colour, which ranges from grey, through dark grey, to black (Fig. 2).

Thin sections revealed that analysed mudstones are generally matrix-supported, with a framework built of quartz, feldspars, and micas, as well as carbonates (Fig. 3a). The matrix is a mixture of clay minerals and clay fractions of framework grains. According to Milliken et al. (2018), mudstones from this part of the Baltic Basin have grains of mainly extrabasinal derivation. The rocks are cemented by clay minerals or rarely by clay-silica or clay-calcareous cement. Fragments of various shells, possibly including bivalves, are also present. All samples contain opaque minerals, which we interpreted to be mostly pyrite.

Observation of the thin sections enabled the recognition of four main structural types in the samples, characterized by different sedimentary structures (Fig. 3b–e), namely:

- type A – mudstones with wavy, parallel, and discontinuous lamination (Fig. 3b);
- type B – mudstones with planar, parallel, and continuous lamination (Fig. 3c);
- type C – massive mudstones (homogeneous, Fig. 3d);
- type D – mudstones with lamination strongly disturbed by bioturbations (Fig. 3e).

Samples having wavy lamination (type A) are composed of elongated lenses of light material (Fig. 3b) that we interpreted as compacted intraclasts. The presence of intraclasts is related to erosion, transport and compaction of surficial muds (Schieber, 2016; Schieber et al., 2010). In the case of samples with planar lamination (Type B), the lamina width may vary from ca. 100–1000 μm and some lamina may be enriched in clay minerals or quartz grains (Fig. 3c). The concentration of quartz and silica is related to the presence of agglutinated foraminifera (Milliken et al., 2018). Homogenous mudstones (type C) are massive, display no lamination, and are characterized by the occurrence of shell detritus (Fig. 3d). Mudstones with signs of bioturbation (type D) are rich in

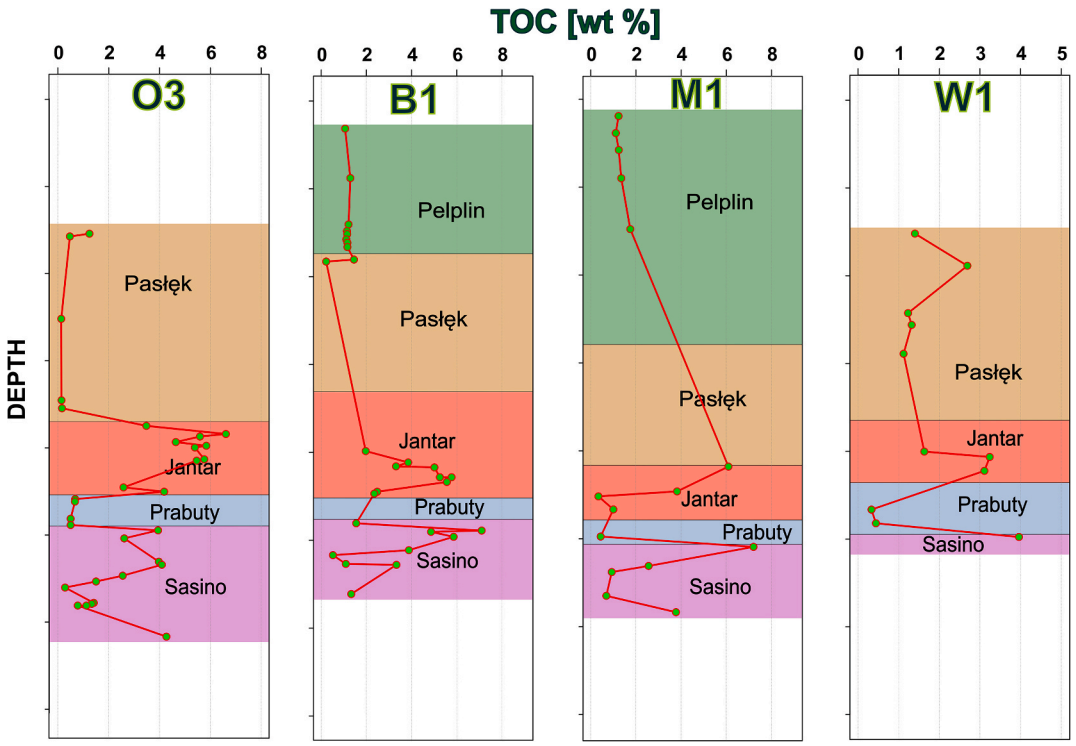

Fig. 6. Vertical profile of TOC concentrations in examined sections of wells O3, B1, M1, and W1.

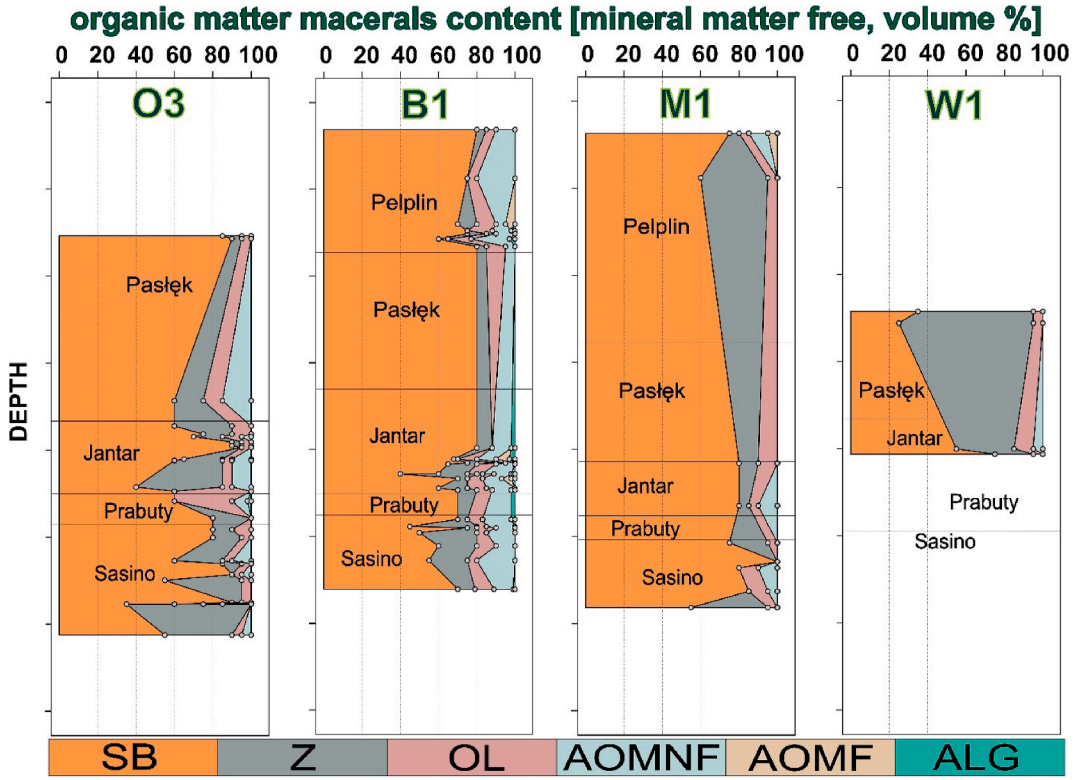

Fig. 7. Vertical changes in the maceral content of organic matter. SB = solid bitumen, Z = zooclasts (mainly graptolites), AOMF and AOMNF = fluorescence and non-fluorescence amorphous organic matter, ALG = alginite, OL = other macerals from liptinite group.

irregular fragments of bright material occurring within a darker matrix (Fig. 3e). The Pelplin Formation is characterized by the presence of type A lamination. The lamination types B and D were found in Prabuty Formation samples, as well as in Jantar and Sasino Formation samples. Type C was observed in samples from the Prabuty and Sasino Formations.

Pyrite concretions are dominated by small, rounded concentrations (up to several μm in diameter) that may be isolated or grouped in thin

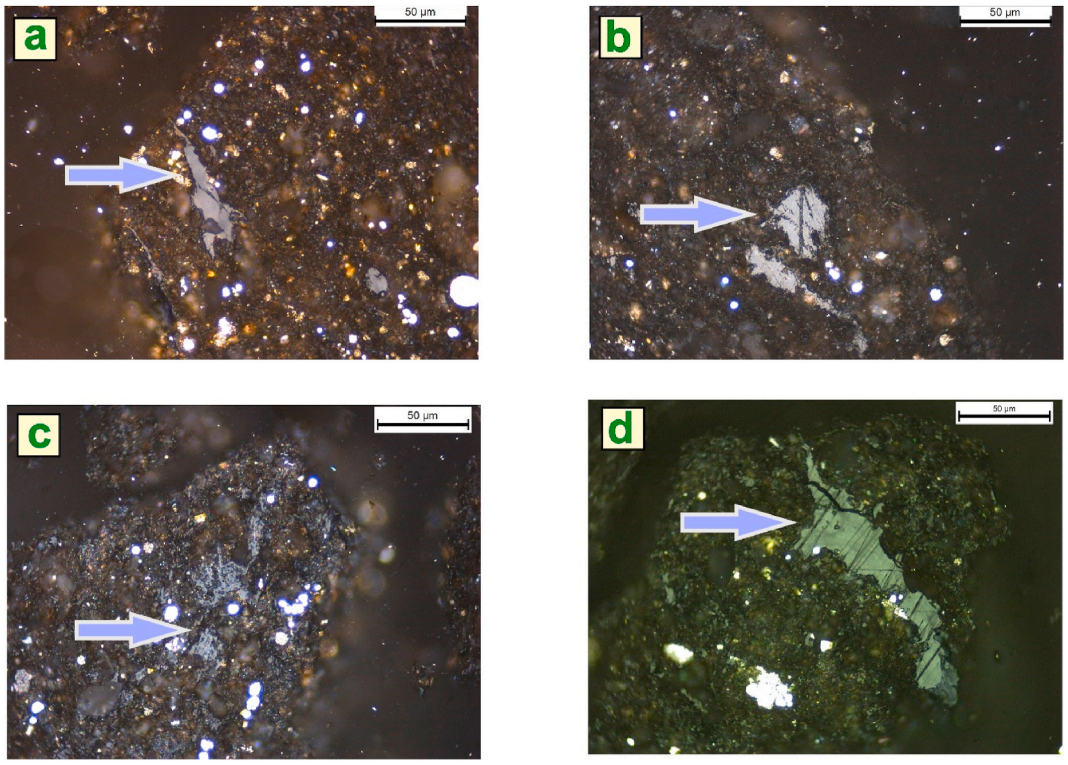

Fig. 8. Examples of solid bitumen fragments filling voids in the mineral matrix of analysed rocks. (a) Homogenous solid bitumen (Sasino Formation), (b and c) granular solid bitumen (Jantar Formation) and (d) anisotropic solid bitumen texture of its surface (Sasino Formation).

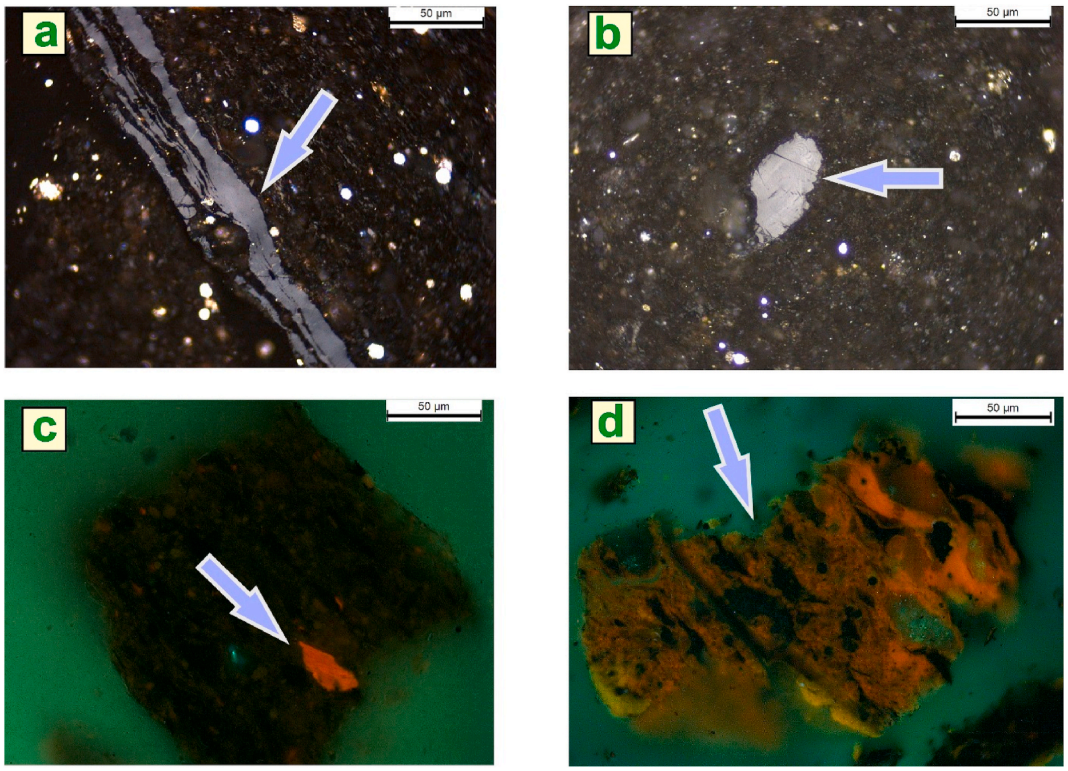

Fig. 9. Fragments of graptolites and alginite particles (Jantar Formation). (a,b) Longitudinal and perpendicular cross sections of graptolites, (c, d) alginite exhibits fluorescence under UV light (colour points to thermal maturity between oil and wet gas windows). (For interpretation of the references to colour in this figure legend, the reader is referred to the Web version of this article.)

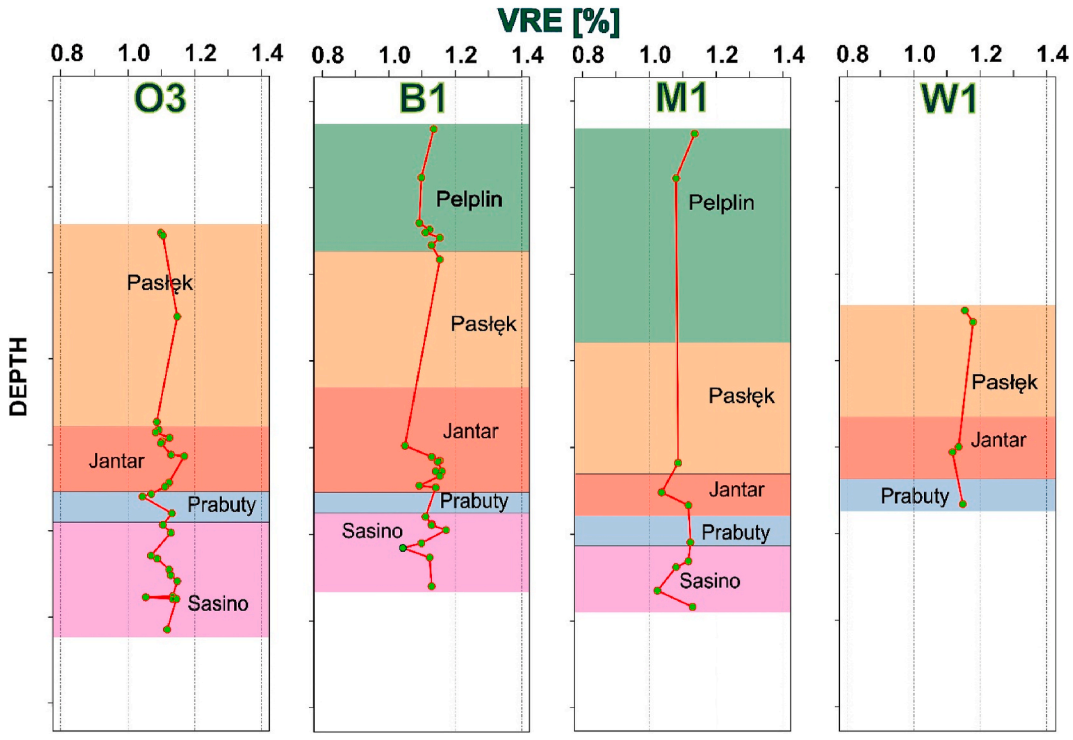

Fig. 10. Vertical changes of organic matter reflectance (measured as solid bitumen reflectance SBRo and recalculated into vitrinite equivalent VRE) in examined sections of wells O3, B1, M1, and W1.

laminae (Fig. 3b), although pyrite sometimes appears as irregular concentrations up to ca. 4 mm in length (Fig. 3d). In some samples from the Prabuty, Jantar, and Sasino Formations, there are visible thick laminae rich in coarse quartz grains (Fig. 3c), whereas samples having higher carbonate contents are usually bright mudstones with argillaceous-calcareous cement (Fig. 3d).

The mineral composition of the samples, determined by XRD, is shown in Fig. 4. The studied mudstones from all four wells are composed mainly of clay minerals ranging from 24.1 to 67.5 wt %—including illite, muscovite, illite-smectite interstratified minerals, kaolinite, and chlorites. The median values of clay mineral content in all analysed formations are similar and range between 43 and 50 wt %. The next important component is quartz, ranging from 19.9 to 65.6 wt %; however, the median amount of quartz falls in the narrow range from 27 to 30 wt % in all lithostratigraphic units. Carbonates (calcite, dolomite, and ankerite) contribute up to 35.6 wt %, but the median values are equal to around 6–10 wt % for the Pelplin, Pasłęk, and Prabuty Formations and 3 wt % for the Jantar and Sasino Formations. The amount of feldspar (both K-feldspar and plagioclase) ranges between 1.2 and 9.9 wt %. The sum of remaining mineral phases (i.e., sulphides, sulphates, Fe-oxyhydroxides, apatite, and anatase) varies from 0 to 16 wt %, though it is usually below 10 wt %. The vertical compositional profiles (Fig. 4) reveal a general mineralogical homogeneity of the suite of samples. However, there are infrequent thin horizons (usually represented only by one or two samples) that are enriched in carbonates or quartz. The latter was also confirmed by the microscopic observations of thin sections (Fig. 3c).

Because the majority of the analysed samples are dominated by clay minerals, on the ternary mineral distribution diagram proposed by Lazar et al. (2015), they fall in the argillaceous mudstone group (Fig. 5). Only two Sasino Formation samples fall into the siliceous mudstones group (Fig. 5a), while a few samples from the Pasłęk, Jantar, and Sasino Formations are siliceous and argillaceous mudstones (Fig. 5b, d). Additionally, two samples from the Prabuty Formation are characterized by compositions typical for the transition from argillaceous to calcareous mudstones (Fig. 5a). There is no correlation between the mineralogical composition and the described diversity of sedimentary structures.

4.2. TOC content and organic petrology

The TOC content of samples ranges from 0.13 to 7.2 wt %. Despite the relatively wide range of TOC, there is no relationship between the depth and the presence of TOC (Fig. 6). The median values of TOC in the mudstones from the Pelplin and Pasłęk Formations are equal to ~1.15–1.2%, while the samples from the Prabuty Formation have median TOC values of ~0.5%. Only the samples from the Jantar and Sasino Formations are characterized by TOC contents above 3 wt % (Fig. 6), with medians of 4.01% and 2.56%, respectively.

Variations in maceral composition in vertical profiles are shown in Fig. 7. Semi-quantitative maceral analysis revealed that OM is dominated by solid bitumen ([SB], from 35 to 90 vol %), where the remaining OM consists mainly of fragments of zooclasts (Z), predominantly graptolites. There is no obvious trend in solid bitumen content among the analysed set of samples (Fig. 7). Solid bitumen often fills cracks and voids (Fig. 8), and its fragments vary in size from a few μm up to ca. 100 μm. The solid bitumen particles are generally homogenous (Fig. 8a), however, fragments having granular (Fig. 8b and c) and anisotropic textures (Fig. 8d) are also present. Graptolites are the second important organic component in the sampled mudstones (Fig. 7), accounting for up to 70 vol %. Usually, however, their content does not exceed 40 vol % (Fig. 7). Graptolites were observed in various cross-sections, from longitudinal, with two branches visible, to perpendicular (Fig. 9a and b), have sizes varying from 50 to 150 μm in length and from 25 to 50 μm in diameter. Other organic macerals present are from the liptinite group (including rare alginite, Fig. 9c and d), as well as amorphous OM (both fluorescent and not).

The thermal maturity of OM, expressed in the VRE scale, was recalculated from the SBR_o using the Jacob equation (Jacob, 1989). After this recalculation, the thermal maturity of the studied samples varies from 1.02 to 1.18% in the VRE scale (Fig. 10). However, the VRE value for the majority of the inspected samples falls in the range between 1.1 and 1.15%. There is no link between the degree of maturity and the

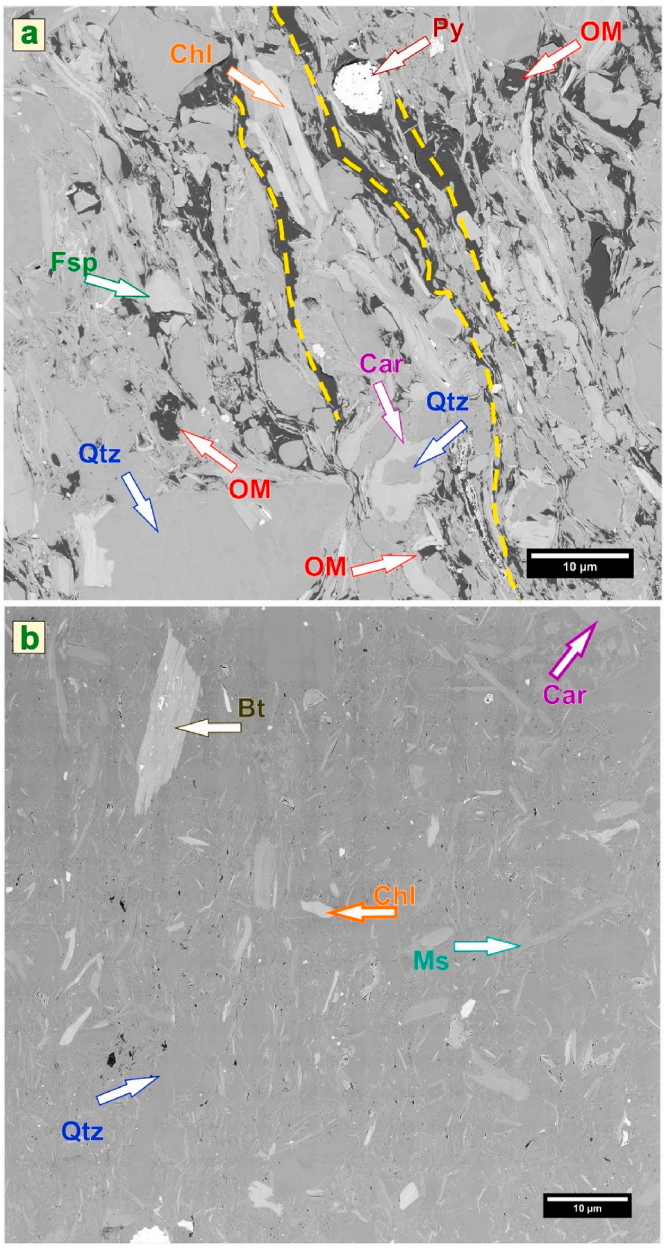

Fig. 11. SEM BSE images of: (a) sample 10 UWR. The framework is quartz, mica, chlorite, and occasionally carbonates and feldspar. Clay mineral flakes are parallel to the sedimentary lamination surface. Please note that organic matter (OM) is present both as isolated patches (red arrows), as well as elongated fulfilments of the voids between minerals (marked by the yellow line) (b) Sample SQ703.3. Framework grains are nearly the same in the case of sample 10 UWR, however, lack of organic matter is easily seen (TOC = 0.52%). A thin section of samples such as SQ703.3 indicate bioturbation, which is confirmed by the lack of parallel arrangement of clay minerals in the SEM BSE image. Mineral abbreviations after Whitney and Evans (2010): Bt-biotite, Chl-chlorite, Fsp-feldspars, Ms-muscovite, Py-pyrite, Qtz-quartz. (For interpretation of the references to colour in this figure legend, the reader is referred to the Web version of this article.)

depth of samples (Fig. 10). Note that the yellow-orange to orange fluorescence colours of alginite visible under the microscope also supports thermal maturity interpreted from reflectance measurements in the studied rocks (Fig. 9c and d). This spectrum of colours specifically points to maturity ~1% in the VRE scale (Hackley and Cardott, 2016; Mastalerz et al., 2018), which suggests the beginning of the late mature stage between the oil and wet gas windows (Mastalerz et al., 2013).

4.3. Microstructure of the studied rocks

A close inspection of the SEM BSE images supports the observations from thin section analysis and XRD measurements and provided more precise information about samples' structure and composition. The framework of the inspected samples comprises subrounded quartz grains, muscovite flakes, but also chlorites, feldspar grains (both potassium and alkali), and carbonate grains (Fig. 11a and b). The diameter of quartz grains seen in SEM BSE images varies from 5 to 30 μm, flakes of chlorite and mica do not usually exceed 20 μm, while feldspar and carbonate grains size fall in the range between 10 and 25 μm (Fig. 11a and b). Occasionally carbonates, mainly dolomite and calcite, create coatings around other framework grains (Fig. 11a). Most of the clay minerals flakes are parallel to each other and define the lamination surface (Fig. 11a). On the other hand, bioturbated samples do not display this kind of clay mineral alignment (Fig. 11b). However, in general, the types of sedimentary structures distinguished in thin sections cannot be detected at the micrometre scale. The analysis of SEM images confirms that the opaque minerals are mainly pyrite (Fig. 11a), although barite and titanium oxide are also occasionally present.

In the analysed suite of samples, OM may be distributed as irregular isolated patches, no bigger than a few micrometres (Fig. 11a). However, the OM is also arranged in an interconnected network, filling voids between minerals and arranged parallel to the sedimentary layering (Fig. 11a). Such an arrangement is probably an effect of the migration of organic substances generated from kerogen through the rock matrix. Because the dimension of OM fragments exceeds the observation field at the selected magnification, we assume that their length must be greater than ca. 60 μm (Fig. 11a). Imaged OM fragments range from generally nonporous (although sometimes with crack-based pores, Fig. 12a) to high porosity (Fig. 12b).

The SEM BSE data allowed us to distinguish different types of pores associated with various components and features of the samples (Fig. 13). This spectrum of porosity types includes (1) pores developed at the edges of rigid minerals (i.e., quartz): pressed into more plastic surroundings (i.e., clay minerals), (2) pores inside the grains, (3) cracks, (4) pores within aggregates of clay minerals, (5) pores within the pyrite framboids, and (6) porosity in OM particles.

The conducted FIB-SEM imaging enabled better insight into the 3-D geometry of the pore networks. Fig. 13 is an example of FIB-SEM reconstruction. It is visible that pore spaces are arranged, in general, in a plane parallel to the lamination surface (Fig. 14c and d). Reconstructed pores can be divided into three categories (Fig. 14c and d): (1) spherical and ellipsoidal isolated (at resolution available in FIB-SEM) pores, (2) elongated pores with ellipsoidal cross-sections, and (3) long interconnected pores with variable diameters and shapes. Pores such as those shown in Fig. 14 are related mainly to clay mineral aggregates or occur within OM fragments.

4.4. Porosity measurements and analysis

4.4.1. Image analysis

For all the samples analysed using SEM BSE, the porosity visible in the images does not exceed 1%, while the porosity values calculated from 3-D FIB-SEM data are ranging from 0 to 2.7% (Tab. A.1; Appendix A). Based on SEM BSE images, we distinguished three types of visible porosity: intraparticle pores (INTRAP) inside framboids of pyrite and voids in carbonates, interparticle pores (INTERP) related to voids between mineral grains and organic matter pores (OMP) developed exclusively within the OM. In these rocks, INTERP porosity is developed mainly between clay mineral flakes, which often form clay mineral aggregates. The contribution of different types of pores to the total detected porosity by means of SEM BSE is shown on a ternary diagram (Fig. 15a). In all mudstone samples, INTERP or OMP dominate (Fig. 15a). The contribution of INTRAP to total porosity is small and ranges from 2 to 10% of the total visible porosity. Six out of nine samples

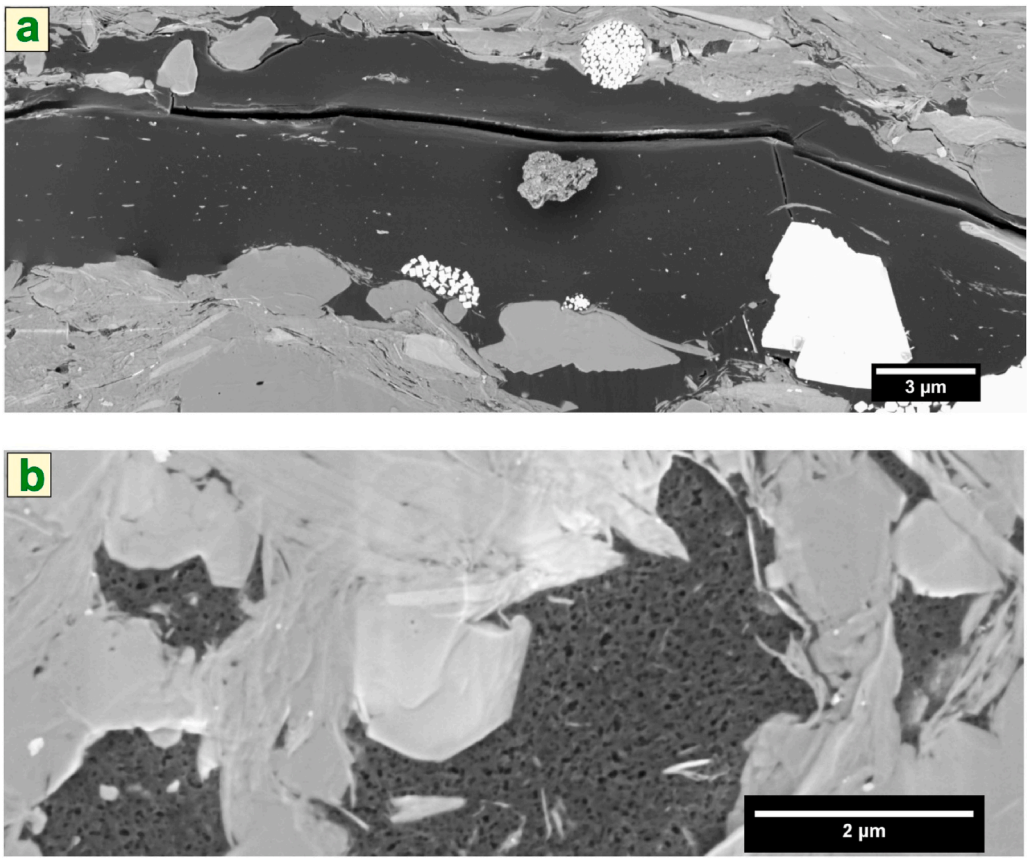

Fig. 12. Different levels of porosity formation in organic matter fragments, from (a) nonporous at the resolving power of the SEM technique (sometimes with visible cracks), (b) to highly porous.

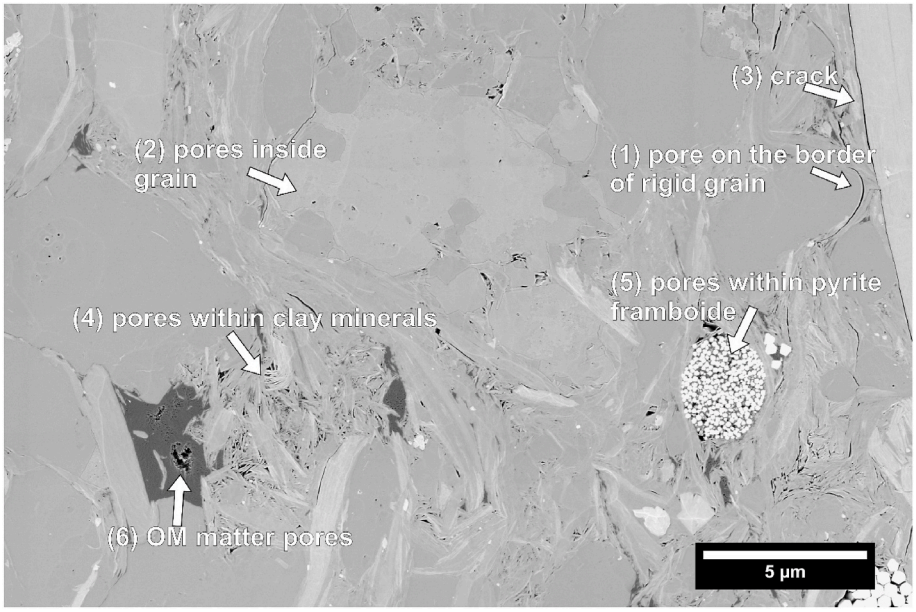

Fig. 13. Different types of pores in examined mudstones.

indicate a pore system controlled by INTERP. Two samples are dominated by OMP, and one sample is characterized by a mixed pore system (Fig. 15a). There is no relationship between OM content and the dominant type of porosity visible in SEM BSE images. (Fig. 15a), which suggests that OM may display a different degree of porosity, owing to its chemical and maceral variability (Curtis et al., 2012).

Based on obtained SEM BSE images, basic descriptive statistics were calculated for the equivalent diameter of pores measurements (Tab. A.2, in Appendix A) and ECDF was prepared for better illustration of the PSD (Fig. 15b). The pore equivalent diameter as detected on SEM BSE images ranges from 10 to 358 nm; however, pores larger than 150 nm occur infrequently (Fig. 15b, Tab. A.2 in Appendix A). The equivalent

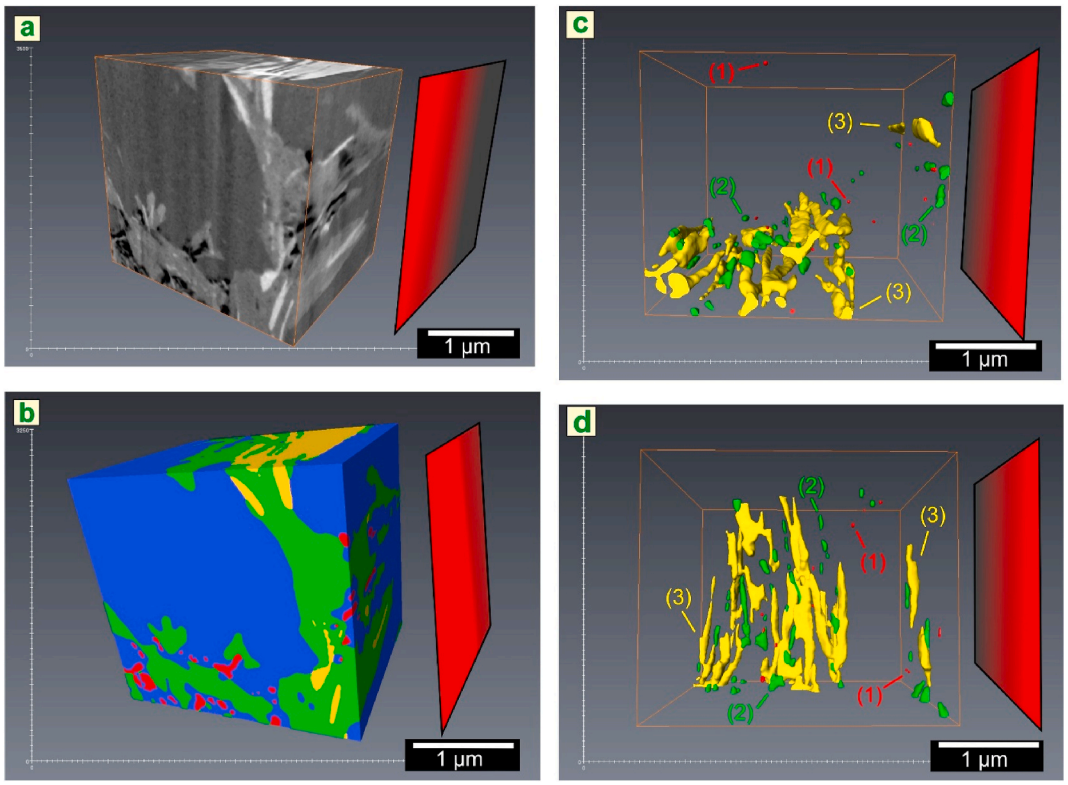

Fig. 14. FIB-SEM reconstruction of sample SQ632.21. (a) 3-D reconstruction of analysed rock volume, (b) rock segmented into most important components: quartz (blue), illite (green), chlorites (yellow), and pore spaces (red), (c, d) porosity divided into (1) small isolated spherical volumes, (2) elongated isolated pores, (3) elongated and connected pores. The red surface indicates lamination arrangement. (For interpretation of the references to colour in this figure legend, the reader is referred to the Web version of this article.)

diameter of half of the voids present in all the samples does not exceed 25 nm, 75% of pores have an equivalent diameter <45 nm and at least 80% of pores are not >50 nm (Tab. A.2, in Appendix A, Fig. 15b). Consequently, all pores fall in the range of mesoporosity. All empirical distribution functions are similar in shape, but there are some subtle differences among the samples. For example, samples 10UWR, 29UWR, and JSOP8 show slightly greater numbers of pores >25 nm, when compared with the rest of the mudstones (Fig. 15b). Moreover, only in the latter two mentioned samples (29UWR and JSOP8), pores >300 nm were detected (Tab. A.2, in Appendix A). On the other hand, two samples (SQ685.57 and SQ703.3) have relatively low values of maximal equivalent pore diameter, up to 85 and 138 nm, respectively (Fig. 15b, Tab. A.2 in Appendix A).

Kernel density estimator curves also signalise the dominance of mesopores (10–50 nm) in the studied samples (Fig. 16). However, samples 10UWR, 29UWR, and JSOP8 display a slightly broader pore size range, reaching up to ca. 100 nm (Fig. 16g, h, i, respectively). This observation is consistent with the empirical data presented in Table A.2 (in Appendix A) and Fig. 15b. Additionally, the modal value of the pore size was calculated for each sample (Fig. 16). The modal values were calculated in three ways: (1) M_{emp} – as an empirical modal value, calculated directly from the collated data; (2) M_{est1} – modal value estimator, calculated by Most Likely Value (mlv) function from the modest package available in the R software, with the application of de Beauville method (Poncet, 2012); (3) M_{est2} – modal value estimator, created by finding the equivalent diameter value corresponding to the maximum value on the KDE curve. The empirical modal value M_{emp} always fits in the narrow range from 10 to 11 nm (Fig. 16). The modal value estimator M_{est1} equals 14–24 nm, while the modal value estimator M_{est2} is in the range of 11–21 nm (Fig. 16).

Both the empirical modal value and its estimators should be considered with care because they are based on observations conducted on a limited and relatively small surface of samples. Moreover, we note that the resolution of the SEM BSE method influences the obtained pore size distribution data, visualised by the ECDF and KDE curves. Nevertheless, there is no doubt that mesopores, (pores not exceeding ca. 50 nm in diameter), prevail among the pores that can be documented by SEM in these mudstone samples.

4.4.2. *Dual liquid porosity*

Performed dual liquid porosity (DLP) measurements enabled us to gain information about the total porosity accessible to water ($Ø_{WIP}$) and maximum porosity accessible to liquid hydrocarbons ($Ø_{KIP}$) in mudstone samples (Topór et al., 2016). The $Ø_{WIP}$ porosity varies from 1.3 to 11.8% (Fig. 17); the median $Ø_{WIP}$ value for the Pelplin, Pasłęk, and Sasino Formations is equal ca. 6.5%, while for the Prabuty and Jantar Formations, the medians are 4.9% and 5.7%, respectively. The $Ø_{KIP}$ porosity values fall between the range of 0.4–10.2% (Fig. 17), but the $Ø_{KIP}$ median value for the Pelplin mudstones is equal to 5.8%, for the Pasłęk 4.2%, while for the remaining lithostratigraphic units, the median $Ø_{KIP}$ measurement is ca. 3.4%.

In the vertical profiles of each well, the values of both $Ø_{WIP}$ and $Ø_{KIP}$ indicate fluctuation, and there is no evident link between porosity and depth (Fig. 17). However, the fluctuation of $Ø_{WIP}$ and $Ø_{KIP}$ follow a similar trend with depth for O3, B1 and M1 wells in the Sasino Formation. This might be connected with variations of TOC amount on the boundary between the Prabuty and Sasino Formations and inside the latter formation (Fig. 6).

4.4.3. *CO_2 and N_2 low-pressure adsorption results*

Low-pressure gas (CO_2 and N_2) adsorption measurements provide information about micro- and mesopore specific volume (V_{DA} and V_{BJH}, respectively), mesopore specific area (S_{BET}), and pore geometry. The range of V_{DA} results in samples varies from 0.007 to 0.018 cm^3/g

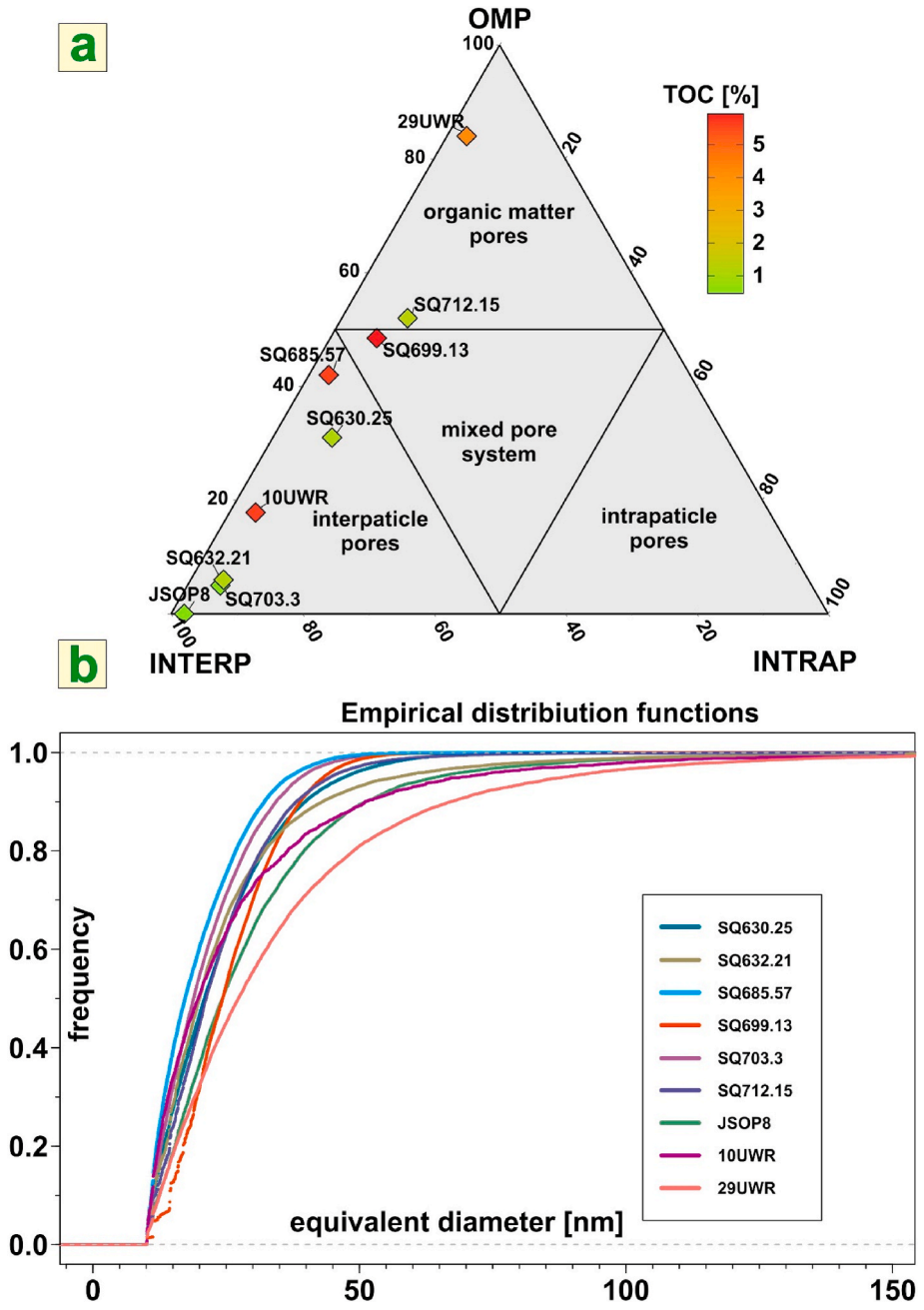

Fig. 15. (a) Ternary diagram illustrating the contribution of different porosity types into total porosity visible in SEM BSE images. TOC concentration in the discussed samples is also shown. (b) Empirical distribution functions showing pore size distribution (PSD) of pores visible in SEM BSE images. Owing to the very small number of pores greater than 150 nm and negligible differences in EDCF functions among the samples, the horizontal scale of the diagram ends at 150 nm.

(Fig. 18a). The median of V_{DA} measurements for all analysed formations varies from 0.01 to 0.013 cm^3/g.

The results of V_{BJH} represent a broader range from 0.019 to 0.054 cm^3/g (Fig. 18a), while the median values of this parameter in each formation fall in the range from 0.03 to 0.046 cm^3/g. Although there is no visible link between the V_{DA} and V_{BJH} and the depth of the sample, both parameters indicate fluctuations, which are, in general, moderately strong or strongly correlated with each other (Fig. 18a). The specific surface area of pores varies among analysed samples from 10.5 to 32.3 m^2/g (Fig. 18b), while the median values are equal from 13.4 m^2/g (Jantar mudstones), through 16–18 m^2/g (Pelplin, Prabuty, and Sasino mudstones), up to 19.6 m^2/g (Pasłęk mudstones).

Moreover, nitrogen adsorption/desorption isotherms allowed us to describe the geometry of the pore systems. Mudstones from all studied lithostratigraphic units have similar adsorption/desorption isotherms (Fig. 19). The isotherms fall, according to the IUPAC classification (Rouquerol et al., 1999; Sing, 1985), in type IIb, and contain hysteresis loop type H3. Referring to the De Boer (1958) classification system, hysteresis loops observed in the mudstone samples can be classified as a combination of types B and D. These shapes are typical for pores between flat, parallel, or nonparallel surfaces. This may be attributed to the dominance of pores developed in clay mineral and their aggregates (Wang et al., 2018).

Nitrogen adsorption analysis revealed the importance of pores having diameters ranging from 2 to 5 nm and ~20–80 nm (Fig. 20). The former is believed to be related to pores located within clay minerals, while the latter is associated with pores within clay minerals aggregates (Kuila et al., 2014b; Kuila and Prasad, 2013; Saidian et al., 2016; Topór

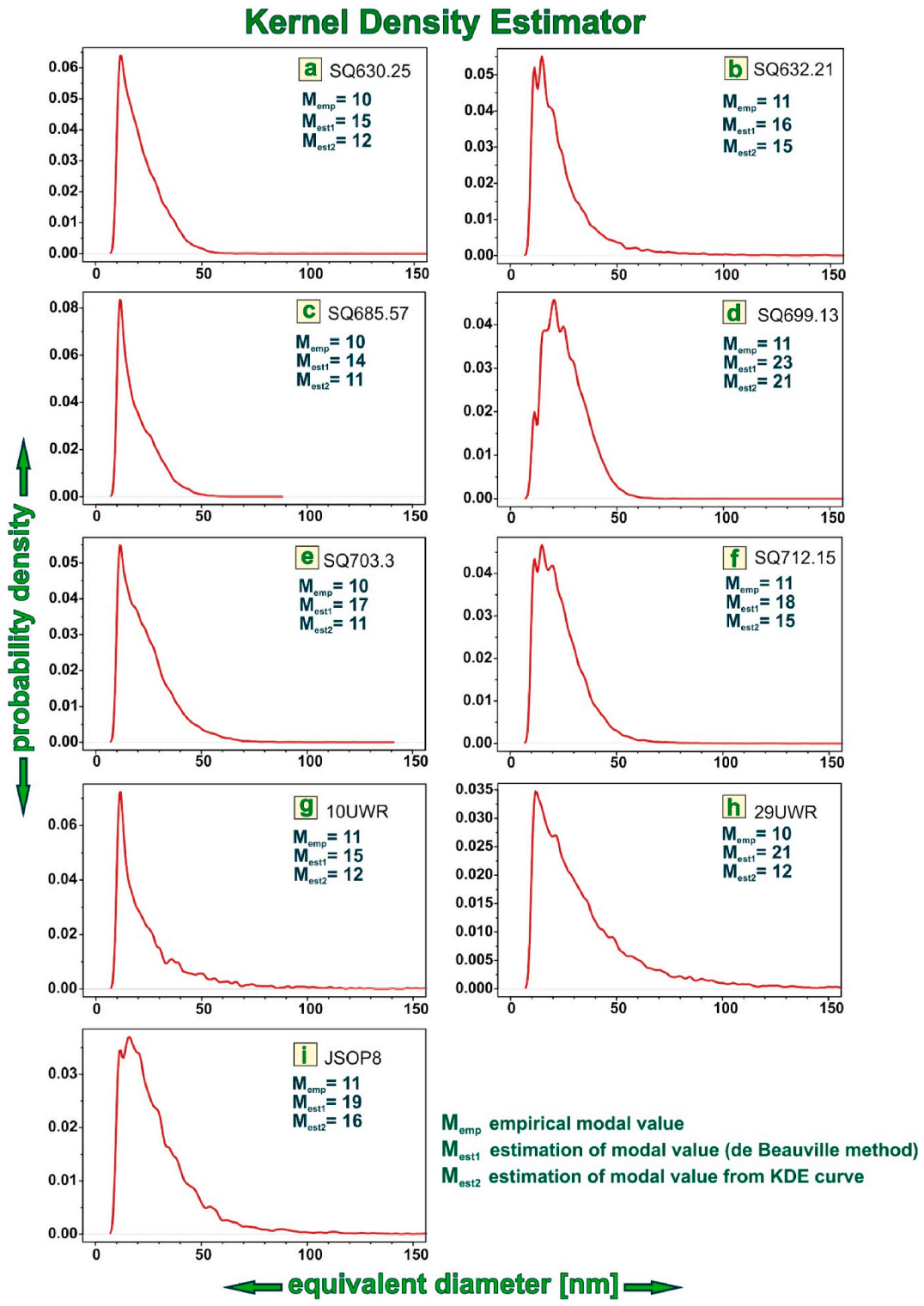

Fig. 16. Kernel density estimators (bandwidth equals 1) based on the measurements of diameters of pores visible in SEM BSE images. All the KDE curves indicate the unimodal shape, however, some secondary peaks may be linked with different types of porosity, i.e. organic matter porosity, cracks, or clay mineral aggregates. Pores greater than 150 nm were omitted because of their negligible meaning and for better clarity of the graphs.

et al., 2017b). The majority of samples display additional peaks around 100 (±20) nm (Fig. 20). These observations are coherent with conclusions drawn based on SEM analysis, thus confirming that mesopores and small macropores developed inside and between clay minerals aggregates have the most significant contribution to the total volume of pore space (excluding large cracks).

No significant differences in adsorption/desorption isotherms and pore size distribution curves were observed between the samples displaying various sedimentary structures. This can be explained by the fact, that porosity in the entire set of samples is developed mainly between and within clay minerals and inside organic matter particles (Fig. 15a).

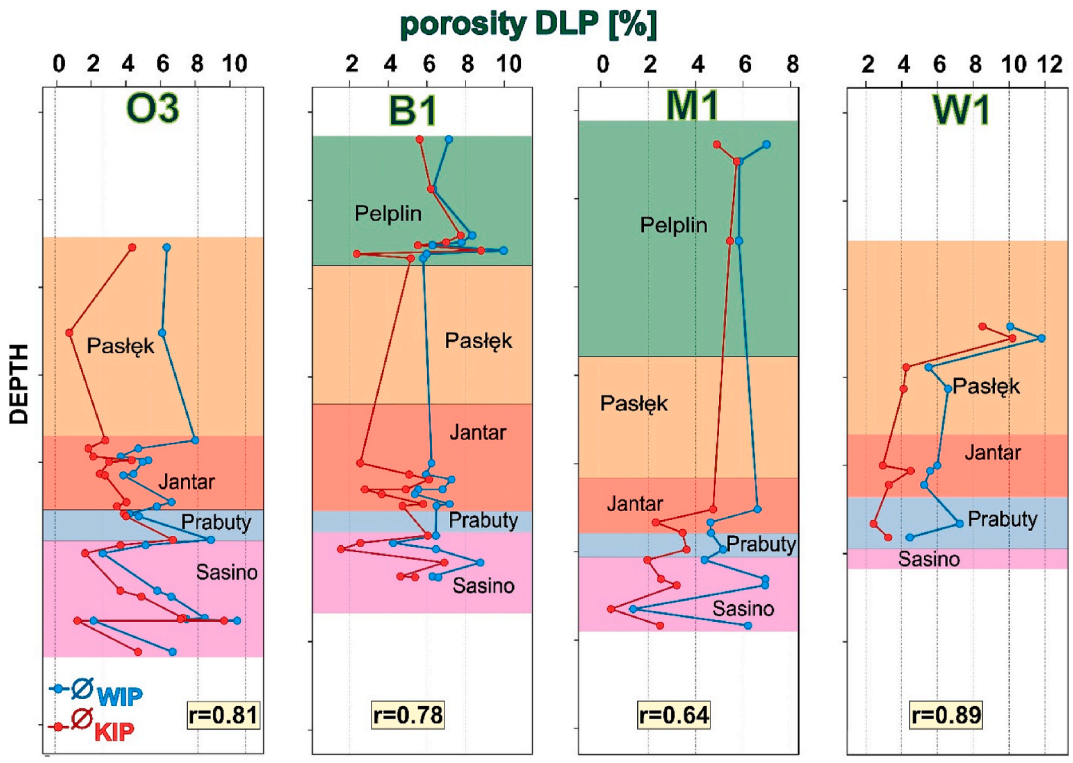

Fig. 17. The vertical changes of $Ø_{WIP}$ and $Ø_{KIP}$ in four studied wells. Please note that $Ø_{WIP}$ values are always larger than $Ø_{KIP}$ values.

5. Discussion

Mineral composition, OM type and its chemical properties, as well as textural and structural features of rocks, control the development of the porosity network in mudstones (i.e., Grathoff et al., 2016; Loucks et al., 2012; Milliken and Olson, 2017; Schieber et al., 2016; Valenza et al., 2013). Our studies, performed for the set of mudstones from the Baltic Basin (N Poland) revealed some factors that govern the size and characteristics of their porosity system. Moreover, the use of several different techniques demonstrates that measurements of porosity and particularly the interpretation of such porosity data in mudstones is still a challenging task. Each technique has its limitations in terms of resolution and the physical and chemical basis of the measurement. In the following section, we compare the results of different techniques and discuss potential causes for the differences.

5.1. The comparison of applied porosity measurements methods

The most noticeable thing about our porosity measurements is that the values obtained using the DLP method (both the $Ø_{WIP}$ and $Ø_{KIP}$), which are methods done for larger sample volumes, are always higher than those resulting from the analysis of SEM BSE and FIB-SEM images (Fig. 21a). This demonstrates the well-known issue that, in the case of mudstones, the application of image analysis will lead to a severe underestimation of total porosity because of the limited resolving power of the electron microscopy techniques. Up to 90% of porosity could be invisible in SEM BSE images, as also shown for Marcellus Shale (Milliken et al. (2013) and the Haynesville Formation (Klaver et al., 2015). On the other hand, the SEM BSE method is very useful in characterizing various types of porosity in terms of 2-D geometry and how this contributes to the total visible porosity.

The DLP techniques provide porosity measurements from a much greater portion of the sample (several cubic centimetres) in contrast to tens of square micrometres in the case of SEM BSE images or hundreds to thousands of cubic micrometres for FIB-SEM data. This makes the DLP method far less affected by the heterogeneity of the sample. Moreover, the DLP measurements also consider all cracks present in the analysed rock volume.

It has been noted by Kelly et al. (2016) that the FIB-SEM should be treated only as a qualitative technique even for analysed samples' volumes that can be considered as large for electron microscopy (up to 5000 μm^3). We want to note that the FIB-SEM data, besides limited resolving power, may also be affected by the choice of the region on the sample's surface and the size of the volume selected to be visualised and analysed. This is likely the reason why samples SQ632.21 and SQ685.57 indicate higher porosity calculated from the FIB-SEM data than from the SEM BES images (Fig. 21a). Regardless of these difficulties, FIB-SEM images obtained from the porous fragments of the rock provide valuable qualitative information about the 3-D arrangement of the pores and their relation to the other rock constituents.

A similar discrepancy can be seen between $Ø_{WIP}$ and $Ø_{KIP}$ results ($\Delta Ø_{WIP\text{-}KIP}$, Fig. 21b), wherein $Ø_{WIP}$ results always show larger values. The majority of samples indicate $\Delta Ø_{WIP\text{-}KIP}$ below 3% or slightly above, while in several samples (JSW9, JSOP15, and JSOP20), this value is near 5%. The $Ø_{WIP}$ and $Ø_{KIP\ are}$ always determined using the same sample, so the difference is related to the fluid used for saturation. This effect stems from different properties (viscosity, wettability, etc.) of these liquids and their distinctively different affinity to clay surfaces (Xu and Dehghanpour, 2014), as well as the size of water and kerosene molecules, which equal ca. 0.28 nm and ca. 1 nm, respectively (Momper, 1978; Nelson, 2009). Note that the studied samples are characterized by a high degree of diagenesis and small amounts of expandable clay minerals, like smectite or illite-smectite mixed layers, so the effect of samples' swelling is marginal and has little impact on porosity values (Topór et al., 2016, and supplementary materials). Effectively, the difference between $Ø_{WIP}$ and $Ø_{KIP}$ reflects incomplete pore saturation by kerosene.

5.2. The implications of the pore size distribution for hydrocarbons flow

The mechanisms of fluid flow through the shales' pore network depend strongly on the size of the pores, since this determines which interactions prevail: between gas molecules or between pore walls and

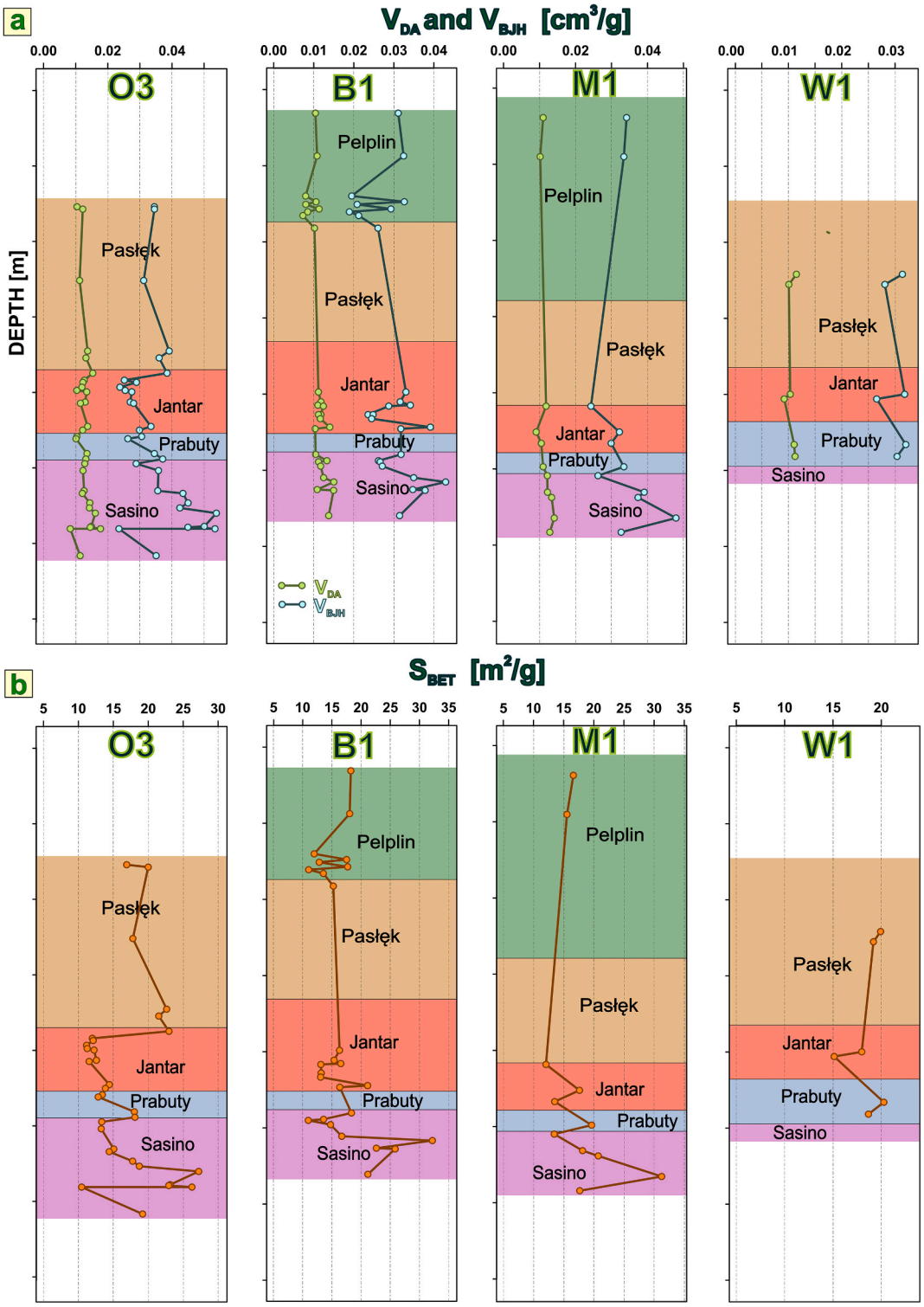

Fig. 18. The vertical diversity of (a) the specific volume of micropores (V_{DA}) and the specific volume of mesopores (V_{BJH}), (b) specific surface area (S_{BET}) of mesopores in the mudstone samples.

gas molecules (Mehmani et al., 2013; Salama et al., 2017). According to numerical simulations provided by Yu et al. (2019), in the case of the smallest pores, with a diameter of ca. 2 nm, interactions between pore walls and gas molecules play the most important role, so that surface diffusion and Knudsen diffusion have the greatest contribution in the total flux. With even a slight increase in the pore size, the importance of surface diffusion decreases and Knudsen diffusion dominates for pores with a diameter of around 6 nm. For pores with diameters of 10 and 16 nm, the contribution of surface diffusion is even lower, but the high share of Knudsen diffusion in the total flow is maintained. Viscous flow becomes of increasing importance at pore sizes of 16 nm and larger. On the other hand, Yang et al. (2021) distinguished the following three types of flow in shales: viscous flow in hydraulic fractures, slip flow in pores macropores, mesopores and micropores and diffusion in micropores. Works of, e.g., Afsharpoor and Javadpour (2016) or Yang et al. (2021) pointed to the role of the slip flow as the predominant type of

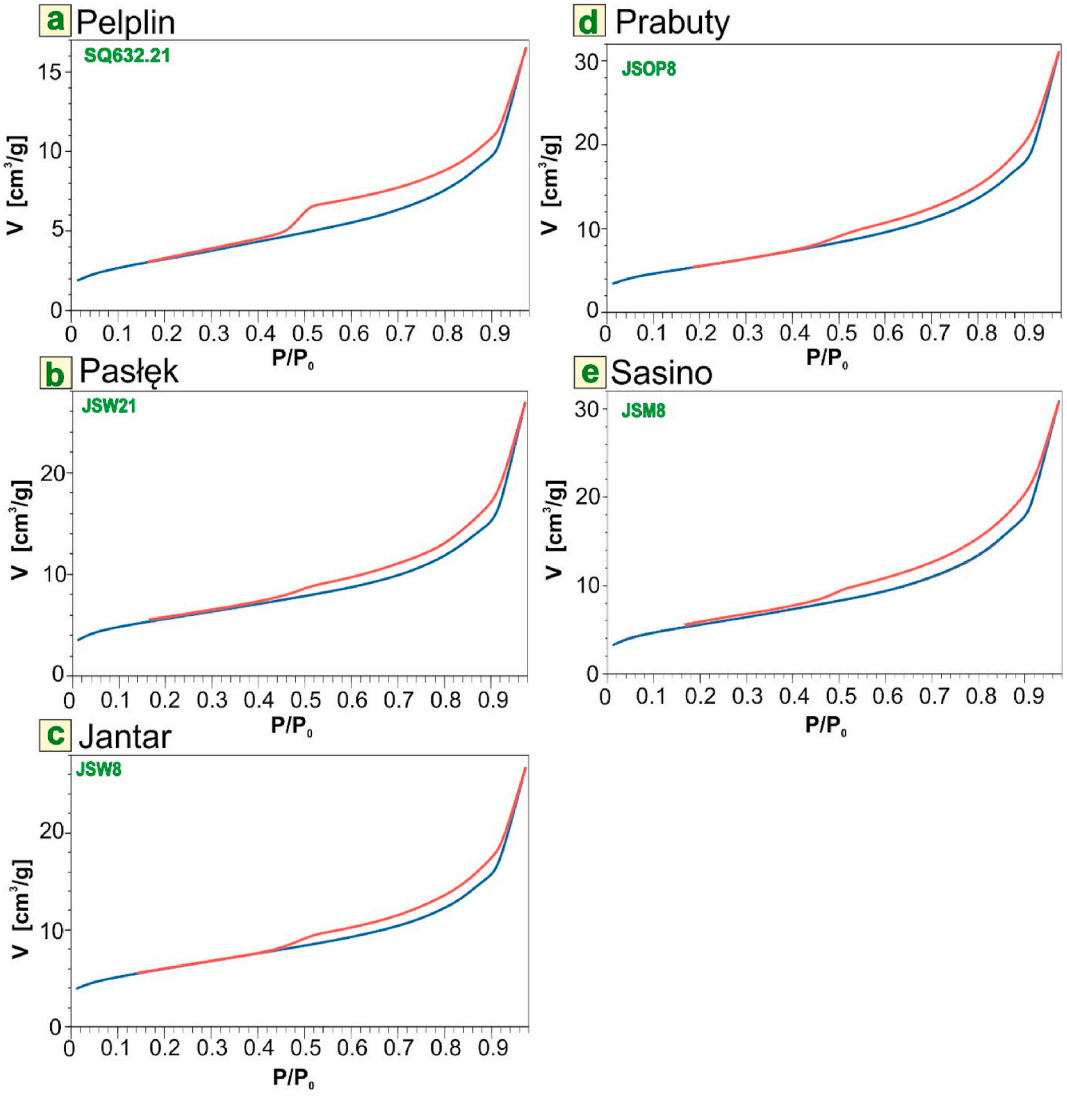

Fig. 19. Representative adsorption/desorption isotherms of nitrogen for samples from: (a) the Pelplin Formation, (b) Pasłęk Formation, (c) Jantar Formation, (d) Prabuty Formation, and (e) Sasino Formation.

flow in shales.

In the studied mudstones (representative for the Pomeranian Baltic Basin), there is a wide array of pore sizes. This suggests that during hydrocarbon production all types of flow mechanisms will occur simultaneously. However, the dominant flow would use preferential paths, which are formed by large and connected pores and cracks. Therefore, viscous flow and also slip flow would have great importance, and especially so in the early stages of the production. The decrease of pressure in the reservoir will later promote diffusion and pores smaller than 10 nm (invisible under SEM, but confirmed in gas adsorption) will have a constantly increasing role in transport (Yu et al., 2019).

We also want to emphasize an additional important aspect of the SEM BSE porosity data. Zhu et al. (2019) showed by combining solvent extraction and gas adsorption studies, that the petroleum flow through early mature shales is possible when the pore diameter is higher than ca. 12 nm. This value is very close to the detection limit of pore size (10 nm) of the SEM BSE data. Any pore volumes of smaller size, invisible in SEM BSE images, most probably will play a minor role in the transport of petroleum. This indicates that the porosity values and pore size distribution from SEM BSE images, even though affected by the resolution of this technique, may be treated as a useful approximation of the minimal porosity available for petroleum migration in the case of mature shales – and the minimal porosity available for matrix flow.

On the other hand, the values of $Ø_{KIP}$ porosity are larger than SEM BSE porosity, partly due to the presence of cracks in the analysed rock cubes. We suggest, that the complementary application of SEM BSE porosity and $Ø_{KIP}$ data can provide the approximation of the range of porosity available for petroleum flow. This knowledge may be important for planning hydrocarbon production and assessing when during production the flow through smaller pores will become more important (Yu et al., 2019).

5.3. The impact of rock composition on porosity

The comparison between the measured porosity values (from DLP and gas adsorption) and primary constituents of the entire set of the studied mudstones rarely show a strong ($r > 0.7$) or even moderate ($r > 0.4$) correlation (Fig. A2, in Appendix A). Furthermore, sample depth does not control porosity. Therefore, we investigated the factors controlling the porosity on a formation level. We focused on statistically significant (probability in a significance test, $p < 0.05$) and at least moderately strong ($r > 0.4$) correlations.

The samples from the Sasino and Jantar Formations indicate the most explicit patterns of relationship between rock composition and properties of the pore network. In these two lithostratigraphic units, the specific surface area of mesopores (S_{BET}) and specific volume of

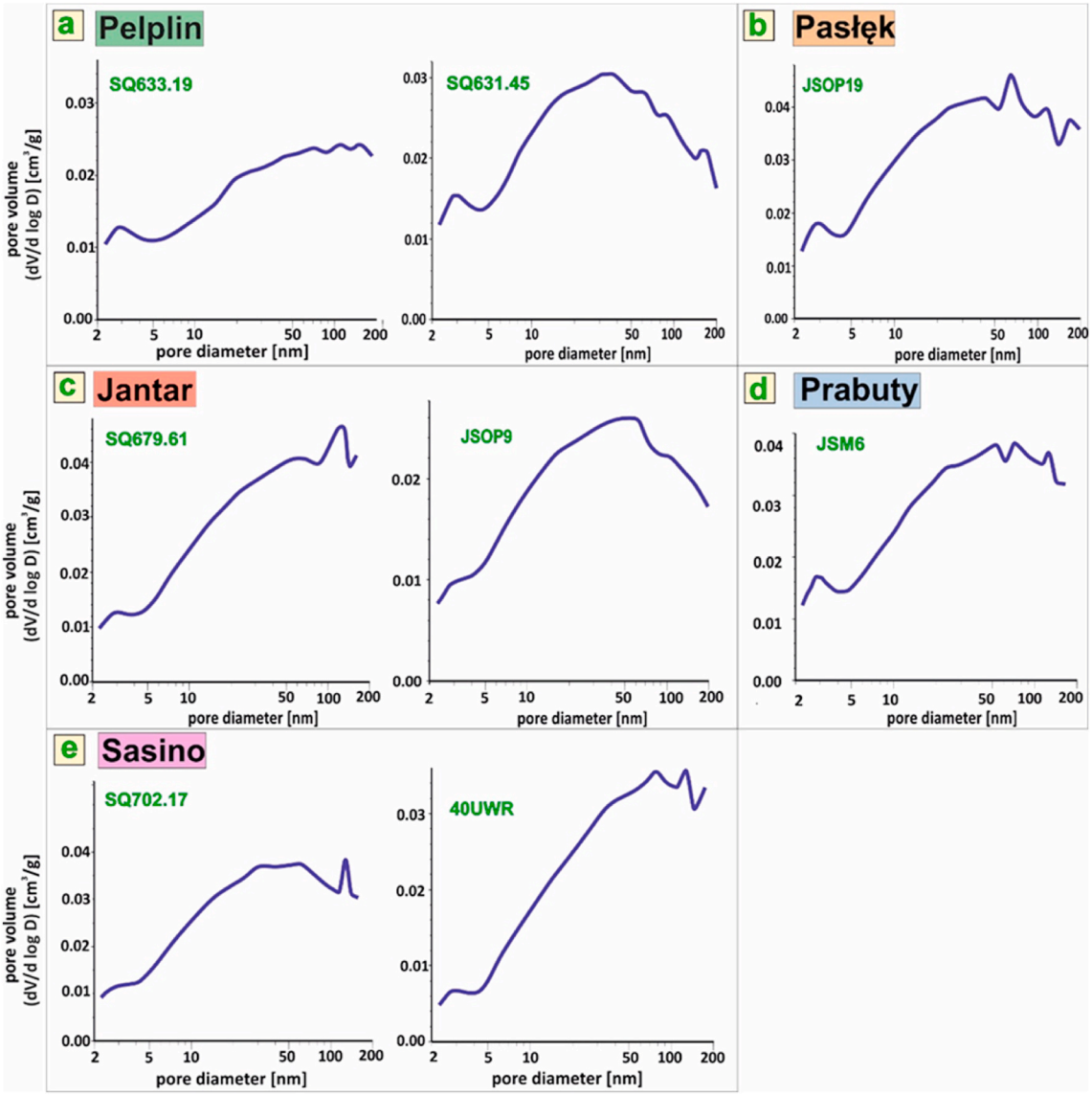

Fig. 20. Representative pore size distribution curves (PSD) based on nitrogen adsorption measurements generated for the samples from: (a) the Pelplin Formation, (b) Pasłęk Formation, (c) Jantar Formation, (d) Prabuty Formation and (e) Sasino Formation.

mesopores (V_{BJH}) are negatively correlated with the amount of TOC (Fig. 22a–d). At the same time, neither the changes in the content of solid bitumen nor subtle fluctuations of OM maturity, play any role in controlling the size of V_{BJH} and S_{BET} (Fig. 22a–d). Considering the fact that OM is present in the examined samples not only as dispersed fragments but also often as connected and elongated solid bitumen that fills voids between minerals (Figs. 8 and 11a), we suggest that observed negative correlation is an effect of pore-clogging by solid bitumen in the Sasino and Jantar Formations. Such phenomenon was described in similar rocks by Valenza et al. (2013), who showed that the specific surface area S_{BET} of mudstones from North American basins increased with the extraction of OM by the mixture of dichloromethane (CH_2Cl_2) and methanol (CH_4OH). The increase of discussed porosity parameters (S_{BET}, V_{BJH}) was also observed by Wei et al. (2014) in New Albany Shale samples after the sequential extraction of OM by dichloromethane and toluene (C_7H_8). In both cited studies, the most significant increase of S_{BET} and V_{BJH} after the removal of OM took place in samples where OM maturity ranged from ~1 to 1.5% in the VRE scale, which is in the range of the late oil/wet gas window (Mastalerz et al., 2018; Tissot and Welte, 2013). Moreover, solid bitumen was the main constituent of the OM in mudstones studied by Valenza et al. (2013) and Wei et al. (2014). The mudstones from the Baltic Basin examined in this research seem to fit this scheme. Solid bitumen is a secondary product of OM transformations (Mastalerz et al., 2018). Therefore, we conclude that petroleum has migrated through the pore network of the mudstones from the studied formations (mostly the Sasino and Jantar Formations) and its residue—solid bitumen—partially clogged the pores in the inorganic rock fabric. This phenomenon was also described by Topór et al. (2017a, 2017b) for Baltic Basin shales from a similar depth and close range of thermal maturity.

The porosity of OM depends on its type (Loucks et al., 2012) and generally increases with maturity (Modica and Lapierre, 2012). For example, solid bitumen can generate pores as a result of secondary cracking (Katz and Arango, 2018). However, some experimental studies revealed, that for rocks rich in solid bitumen, there is a possible reduction of porosity not only between mineral grains but also in OM itself owing to the generation and migration of newly formed hydrocarbons. This effect was observed especially for mudstones characterized by the thermal maturity equal to ca. 0.9% in the VRE scale (Chen and Xiao, 2014). In all the studied mudstones from the Jantar and Sasino Formations, OM maturity (VRE) ranges from ~1 to 1.2%. Solid bitumen in this interval of maturity is not only prone to clogging pores between

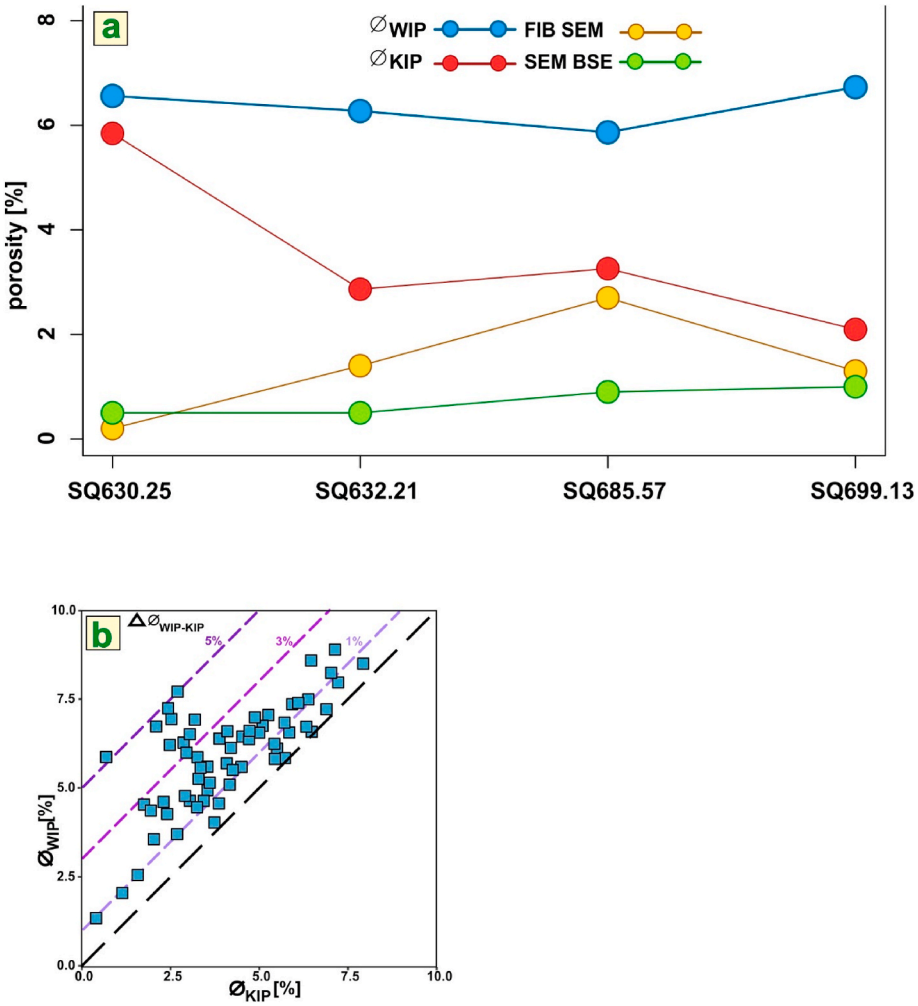

Fig. 21. Comparison of porosity measurements. (a) Porosity values calculated from SEM BSE and FIB-SEM images, as well as results of the DLP method compared for the same samples (wells B1 and O3), (b) $Ø_{WIP}$ and $Ø_{KIP}$ porosity values. Please note that $Ø_{WIP}$ values are always larger than $Ø_{KIP}$ values.

minerals but also tends to have low porosity itself (Chen and Xiao, 2014; Modica and Lapierre, 2012; Valenza et al., 2013; Wei et al., 2014). This is consistent with the SEM BSE data showing that only some fragments of OM have abundant pores (Fig. 12). We conclude that in the studied set of samples, the size and generation of porosity within OM cannot compensate for the effect of pore-clogging, at least at the maturity level studied. This is consistent with the observations of İnan et al. (2018), who suggested that bitumen migrated in the intergranular space, and only minor porosity was formed in solid bitumen fragments for argillaceous mudstone in the oil/early gas window stage. In contrast, works of Yang et al. (2019, 2016) performed for the Silurian shales from the Sichuan Basin showed that porosity increased with the amount of OM in shales, but thermal maturity of those rocks varied between 1.8 and 2.5% in the VRE scale, which is significantly more mature than that of samples used in our research.

Because OM may host microporosity (Chalmers et al., 2012; Clarkson et al., 2013) we could also expect a correlation between TOC content and V_{DA} values in the case of lithostratigraphic units having the greatest TOC diversity (Jantar and Sasino Formations); however, we cannot make such a statement for our set of samples (Fig. 22e and f). The correlations between TOC and V_{DA} are weak and statistically insignificant. We conclude that microporosity in the studied set of mudstones is not particularly well developed in OM, which most probably stems from its thermal maturity.

Our data (Fig. 23) shows that other components controlling the porosity of the studied mudstones are the 2:1 layer type Al-rich clay minerals (I + S: illite, smectite, and interstratified illite-smectite). Their impact is especially reflected in the positive and significant correlations between I + S concentration and the micropores' specific volume V_{DA} in samples from the Pasłęk and the Jantar Formations (Fig. 23a and b). Analogous, positive correlations were also observed for I + S content and specific surface area S_{BET} measured in samples from the Pasłęk and the Prabuty Formations (Fig. 23c and d). The samples from the Prabuty Formation form two clusters, which differ strongly in I + S content and S_{BET} values. The amount of I + S minerals also has a similar impact on the size of micropores' specific volume V_{BJH} in the case of mudstones from the same two formations (Fig. 23e and f).

The importance of the relationship between the amount of clay minerals and mudstones' porosity was reported in many studies (Clarkson et al., 2013; Kuila et al., 2014b; Kuila and Prasad, 2013). Moreover, the SEM BSE images of the mudstones in this study also show that porosity is strongly related to clay minerals. The development of pores within and between the clay mineral aggregates is particularly important when the mudstones are low in OM, like those from the Pasłęk and the Prabuty Formations. In addition, the amount of carbonates in mudstones from the Prabuty Formation influences the specific volumes (V_{DA} and V_{BJH}) of micro- and mesopores and, to a lesser degree, the specific surface area of mesopores (S_{BET}, Fig. 24a–c). Logically, the higher concentrations of carbonates decrease in the amount of clays, which should be followed by the reduction of porosity.

The Pelplin Formation samples are an interesting and unresolved case concerning controls on porosity. The gas adsorption data for these

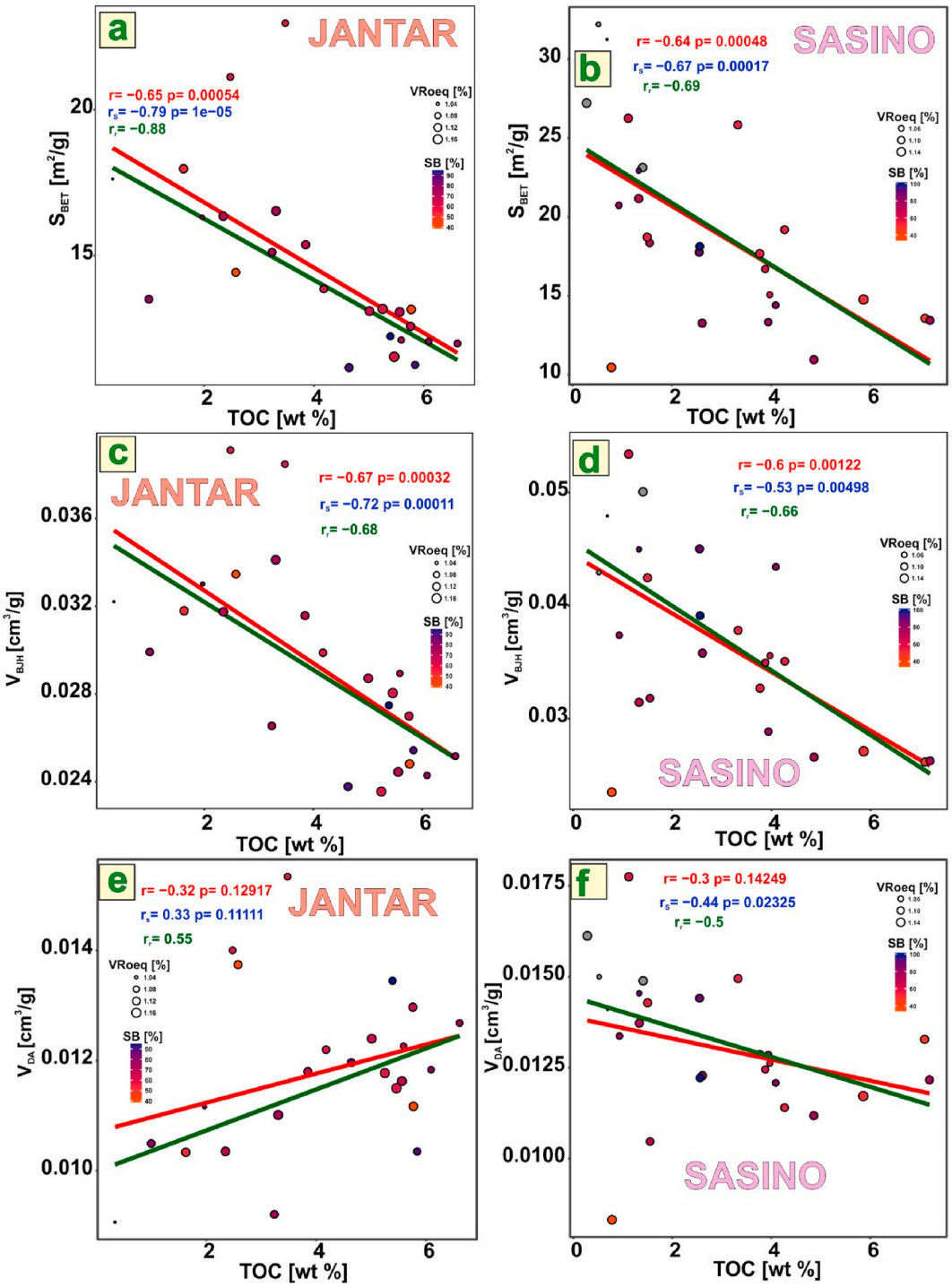

Fig. 22. Correlations between the amount of organic matter (expressed in wt % of TOC) and (a, b) the specific surface area S_{BET}; (c, d) mesopore specific volume V_{BJH}; and (e, f) micropore specific volume V_{DA} in the mudstones from the Jantar and the Sasino Formations. r = Pearson's correlation coefficient, r_S = Spearman's rank correlation coefficient, p = probability in a significance test, significance level $\alpha = 0.05$, r_r = robust linear regression coefficient.

samples are clustered into two groups that show relatively lower and higher values of S_{BET}, V_{DA}, and V_{BJH} (Fig. 24d). Moreover, gas adsorption results do not correlate with TOC, quartz, or clay mineral content. The structural and textural factors also must be excluded because the Pelplin Formation is quite homogenous, and all the samples represent similar wavy, continuous, and planar lamination (Fig. 3b).

Finally, the mineral composition of analysed samples has an impact on their stiffness, and thus also on their reservoir quality. We note that all the studied samples are matrix-supported and are rich in clay minerals. Mudstones like this may not have sufficient stiffness; however, the exception may be horizons having increased amounts of silica (Milliken et al., 2018), like in several mudstones found in our sample set (Fig. 3c).

6. Conclusions

The understanding of porosity and pore size distribution is important for reconstructing migration pathways of hydrocarbons present within

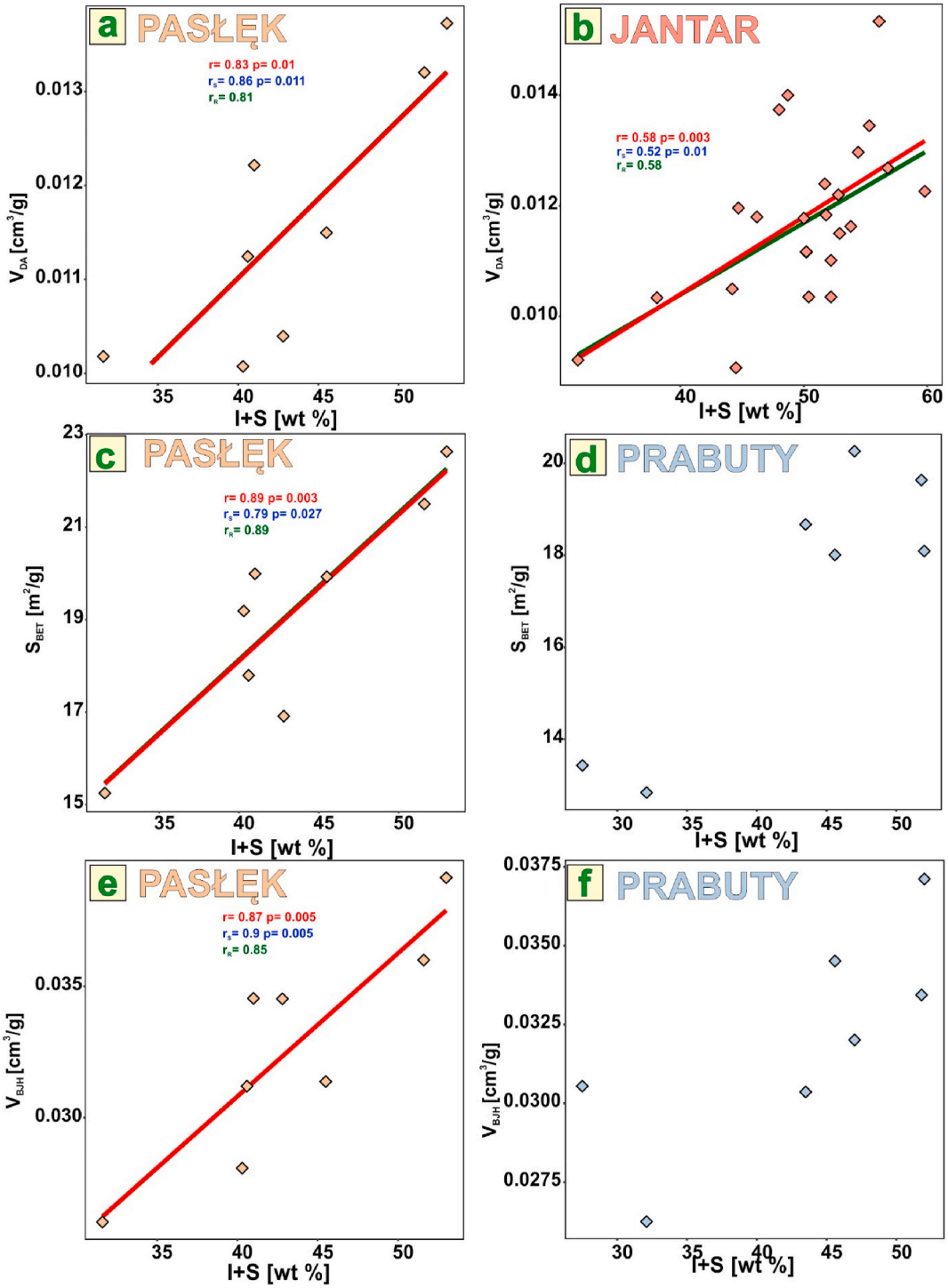

Fig. 23. Correlations between the concentration of selected clay minerals (I + S) and (a, b) the specific surface area SBET; (c, d) mesopore specific volume V_{BJH}; and (e, f) micropore specific volume V_{DA} in the mudstones representing the Pasłęk, Jantar, and Prabuty Formations. Because the samples from the Prabuty Formation are clustered, we resigned from the trend line and correlations coefficients.

fine-grained mudstones. Moreover, having an accurate assessment of the pore volume allows assessing the hydrocarbon storage capacity. This knowledge may be used both in hydrocarbon exploration and production, as well as geological waste storage and carbon dioxide sequestration. In this study, we used a wide array of methods at multiple scales to obtain new information about the porosity of Ordovician and Silurian mudstones from the Baltic Basin (N Poland). Our data generated on mudstones from the Baltic Basin may be useful in studying properties of other mudstones, especially those of Ordovician and Silurian age and with a similar thermal maturity level (between the oil and wet gas window, 1–1.2% VRE).

Our data show that one of the most important factors controlling porosity in such mudstones is the nature of organic matter (amount, type and thermal maturity). At the maturity ~1.0–1.2% VRE, if the solid bitumen is the prevailing organic matter component, it can actually cause a reduction of mesoporosity and, thus, restrict flow paths for hydrocarbons. In turn, microporosity in these formations is not solely related to organic matter but is related to a combination of organic

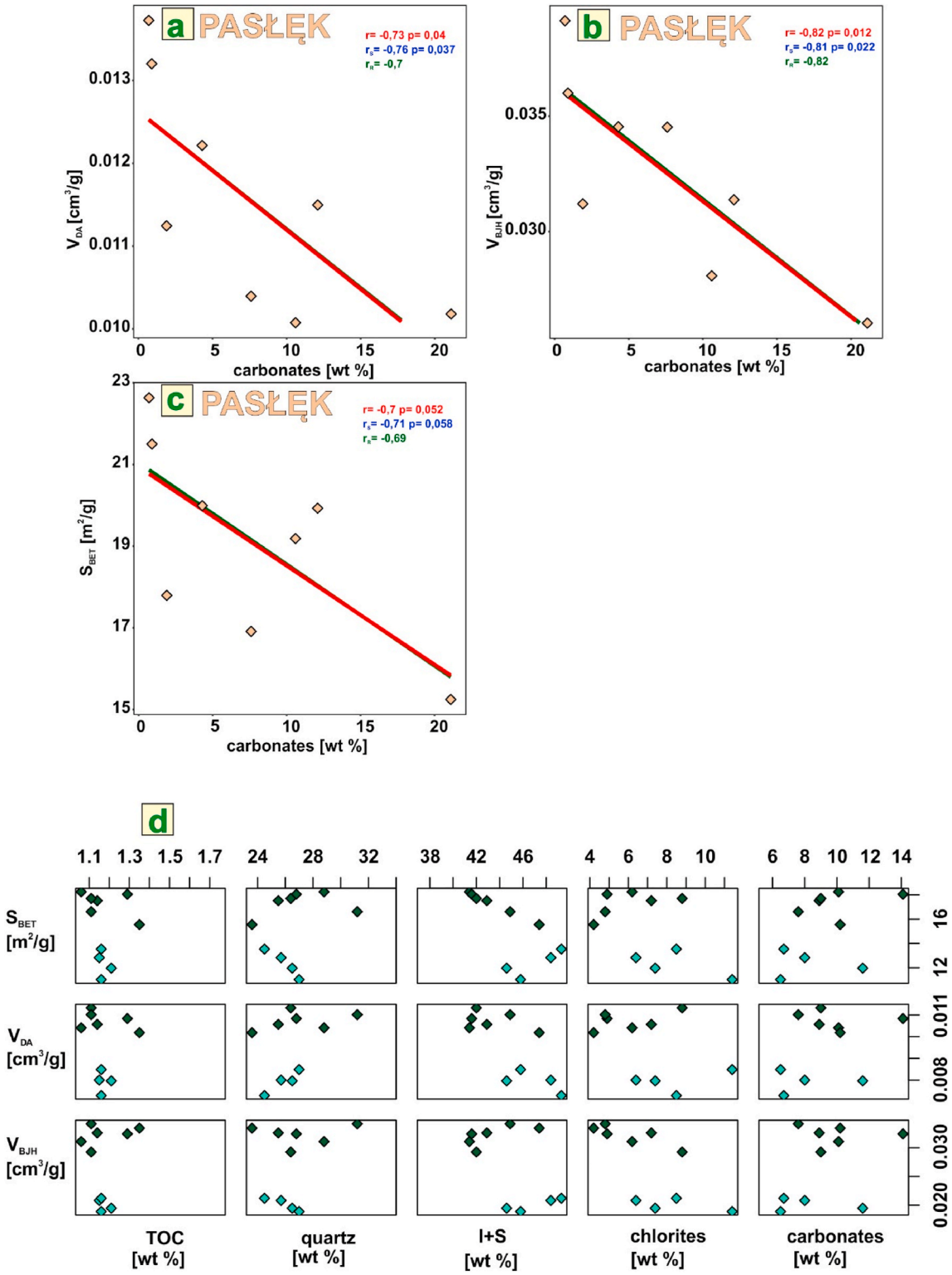

Fig. 24. Correlations between the concentration of carbonates and (a) the specific surface area SBET; (b) mesopore specific volume V_{BJH}; and (c) micropore specific volume V_{DA} in the examined mudstones from the Prabuty Formation (carbonate minerals seem to have impregnated the rocks and, therefore, reduce porosity); (d) the studied set of Pelplin mudstones can be divided into two groups that differ by gas adsorption results, however, these results do not indicate any correlations with primary rock constituents.

matter and clay mineral content. This is even more important since the TOC content is usually seen as a positive parameter when considering hydrocarbon exploration from unconventional reservoirs. However, when considering rocks having high amounts of solid bitumen and thermal maturity on a level of 1–1.2% VRE (like those studied here), we show the potential for limited porosity due to the pore-clogging effect, which may lead to more difficult hydrocarbon extraction. Therefore, organic matter maturity and types of prevailing macerals, in addition to TOC, should be taken into account in defining the prospective zones for hydrocarbon exploitation in mudstones basins. The pore-clogging effect

might also be an important factor limiting the CO_2 sequestration potential of the studied rocks.

Secondly, this study has also important implications for the selection of analytical techniques to measure mudstone porosity and interpreting porosity data generated by various techniques. The comparison of porosity results calculated based on the electron microscopy images with dual liquid porosity (DLP) measurements indicates that both SEM BSE and FIB-SEM techniques have limited capability in the detection of the porosity of mudstones. Both methods provide underestimated porosity values owing to their limited resolution. However, the combination of these methods is quite powerful. The SEM BSE images offer valuable information about types of porosity and potential hydrocarbon migration paths. The pore size distribution data obtained from the SEM BSE images and low pressure gas adsorption reveal the domination of mesopores and small macropores (up to only 80–100 nm). Porosity data from the SEM BSE images are useful approximation of the minimal porosity available for matrix flow, which becomes of importance during the later stages of petroleum production. In contrast, the DLP data provide an estimate of the upper porosity bound, including (micro-) cracks. The representative data type for flow will depend on reservoir pressure conditions and flow regime. The combination of SEM BSE and DLP data enables the estimation of the complete range and size of porosity available for petroleum flow. It underlines the need to apply a broad spectrum of complementary methods that enable the fullest possible characterization of mudstones' pore network.

Declaration of competing interest

The authors declare that they have no known competing financial interests or personal relationships that could have appeared to influence the work reported in this paper.

Acknowledgements

This research was performed in the framework of the ShaleSeq project (Physicochemical effects of CO_2 sequestration in the Pomeranian gas-bearing shales) funded/co-funded from Norway Grants in the Polish-Norwegian Research Programme operated by the National Center for Research and Development, grant no. POL-NOR/234198/100/2014 and in the framework of the ShaleMech project (an integrated geomechanical investigation to enhance gas extraction from the Pomeranian shale formations) funded from BlueGas - Polish Shale Gas Program by the National Center for Research and Development, grant no. BG2/ShaleMech/14.

Mastalerz's contribution is based upon work supported by the U.S. Department of Energy, Office of Science, Office of Basic Energy Sciences, Chemical Sciences, Geosciences, and Biosciences Division under Award Number DE-SC0006978. P. Słomski was also supported by internal PGI-NRI project no. 62.9012.2064.00.0. A. Pluymakers is currently supported by the Dutch Foundation for Scientific Research (NWO) (No. 016.Veni.181.036). We would like to thank the Polish Oil and Gas Company for providing the samples used in this study and the Physics of Geological Processes Group at the University of Oslo for enabling access to Avizo © software.

Appendices A and B. Supplementary data

Supplementary data to this article can be found online at https://doi.org/10.1016/j.marpetgeo.2021.105328.

Credit author statement

Piotr Słomski: Conceptualization, Investigation, Visualization, Data curation, Writing – original draft, Writing – review & editing, Validation, Jacek Szczepański: Conceptualization, Writing – review & editing, Resources, Tomasz Topór: Conceptualization, Writing – review & editing, Resources, Maria Mastalerz: Conceptualization, Investigation, Writing – review & editing, Resources, Anne Pluymakers: Writing – review & editing, Arkadiusz Derkowski: Writing – review & editing, Resources, Tomasz Wojciechowski: Resources.

References

Afsharpoor, A., Javadpour, F., 2016. Liquid slip flow in a network of shale noncircular nanopores. Fuel 180, 580–590. https://doi.org/10.1016/j.fuel.2016.04.078.

Bu, H., Ju, Y., Tan, J., Wang, G., Li, X., 2015. Fractal characteristics of pores in non-marine shales from the Huainan coalfield, eastern China. J. Nat. Gas Sci. Eng. 24, 166–177. https://doi.org/10.1016/j.jngse.2015.03.021.

Chalmers, G.R., Bustin, R.M., Power, I.M., 2012. Characterization of gas shale pore systems by porosimetry, pycnometry, surface area, and field emission scanning electron microscopy/transmission electron microscopy image analyses: examples from the Barnett, Woodford, Haynesville, Marcellus, and Doig units. AAPG Bull. 96, 1099–1119. https://doi.org/10.1306/10171111052.

Chen, J., Xiao, X., 2014. Evolution of nanoporosity in organic-rich shales during thermal maturation. Fuel 129, 173–181. https://doi.org/10.1016/j.fuel.2014.03.058.

Clarkson, C.R., Solano, N., Bustin, R.M., Bustin, A.M.M., Chalmers, G.R.L., He, L., Melnichenko, Y.B., Radliński, A.P., Blach, T.P., 2013. Pore structure characterization of North American shale gas reservoirs using USANS/SANS, gas adsorption, and mercury intrusion. Fuel 103, 606–616. https://doi.org/10.1016/j.fuel.2012.06.119.

Cooper, J., Stamford, L., Azapagic, A., 2016. Shale gas: a review of the economic, environmental, and social sustainability. Energy Technol. 4, 772–792. https://doi.org/10.1002/ente.201500464.

Curtis, M.E., Cardott, B.J., Sondergeld, C.H., Rai, C.S., 2012. Development of organic porosity in the Woodford Shale with increasing thermal maturity. Int. J. Coal Geol. 103, 26–31. https://doi.org/10.1016/j.coal.2012.08.004.

Dayal, A.M., 2017. Shale. In: Shale Gas: Exploration and Environmental and Economic Impacts. Elsevier, pp. 1–11. https://doi.org/10.1016/B978-0-12-809573-7.00001-9.

De Boer, J.H., 1958. Structure and Properties of Porous Materials. Butterworths Scientific Publications, London.

Grathoff, G.H., Peltz, M., Enzmann, F., Kaufhold, S., 2016. Porosity and permeability determination of organic-rich Posidonia shales based on 3-D analyses by FIB-SEM microscopy. Solid Earth 7, 1145–1156. https://doi.org/10.5194/se-7-1145-2016.

Grotek, I., 2006. Dojrzałość termiczna materii organicznej z utworów pokrywy osadowej pomorskiego odcinka TESZ, basenu bałtyckiego oraz obszarów przyległych. Pr. Panstwowego Inst. Geol. (1988) 186, 253–270.

Hackley, P.C., Cardott, B.J., 2016. Application of organic petrography in North American shale petroleum systems: a review. Int. J. Coal Geol. 163, 8–51. https://doi.org/10.1016/j.coal.2016.06.010.

Hemes, S., Desbois, G., Urai, J.L., Schröppel, B., Schwarz, J.-O., 2015. Multi-scale characterization of porosity in Boom Clay (HADES-level, Mol, Belgium) using a combination of X-ray μ-CT, 2D BIB-SEM and FIB-SEM tomography. Microporous Mesoporous Mater. 208, 1–20. https://doi.org/10.1016/j.micromeso.2015.01.022.

Houben, M.E., Desbois, G., Urai, J.L., 2013. Pore morphology and distribution in the Shaly facies of Opalinus Clay (Mont Terri, Switzerland): insights from representative 2D BIB–SEM investigations on mm to nm scale. Appl. Clay Sci. 71, 82–97. https://doi.org/10.1016/j.clay.2012.11.006.

İnan, S., Al Badairy, H., İnan, T., Al Zahrani, A., 2018. Formation and occurrence of organic matter-hosted porosity in shales. Int. J. Coal Geol. 199, 39–51. https://doi.org/10.1016/j.coal.2018.09.021.

Jacob, H., 1989. Classification, structure, genesis and practical importance of natural solid oil bitumen ("migrabitumen"). Int. J. Coal Geol. 11, 65–79. https://doi.org/10.1016/0166-5162(89)90113-4.

Jiang, Z., Zhang, W., Liang, C., Wang, Y., Liu, H., Chen, X., 2016. Basic characteristics and evaluation of shale oil reservoirs. Pet. Res. 1, 149–163 https://doi.org/Kuil.

Karnkowski, P.H., 2007. Petroleum provinces in Poland. Przeglad Geol. 55, 1061–1167.

Katz, B.J., Arango, I., 2018. Organic porosity: a geochemist's view of the current state of understanding. Org. Geochem. 123, 1–16. https://doi.org/10.1016/j.orggeochem.2018.05.015.

Kelly, S., El-Sobky, H., Torres-Verdín, C., Balhoff, M.T., 2016. Assessing the utility of FIB-SEM images for shale digital rock physics. Adv. Water Resour. 95, 302–316. https://doi.org/10.1016/j.advwatres.2015.06.010.

Kiersnowski, H., Dyrka, I., 2013. Ordovician-Silurian shale gas resources potential in Poland: evaluation of Gas Resources Assessment Reports published to date and expected improvements for 2014 forthcoming Assessment. Przeglad Geol. 61, 639–656.

Klaver, J., Desbois, G., Littke, R., Urai, J.L., 2015. BIB-SEM characterization of pore space morphology and distribution in postmature to overmature samples from the Haynesville and Bossier Shales. Mar. Petrol. Geol. 59, 451–466. https://doi.org/10.1016/j.marpetgeo.2014.09.020.

Kuila, U., Prasad, M., 2013. Specific surface area and pore-size distribution in clays and shales. Geophys. Prospect. 61, 341–362. https://doi.org/10.1111/1365-2478.12028.

Kuila, U., McCarty, D.K., Derkowski, A., Fischer, T.B., Prasad, M., 2014a. Total porosity measurement in gas shales by the water immersion porosimetry (WIP) method. Fuel 117, 1115–1129. https://doi.org/10.1016/j.fuel.2013.09.073.

Kuila, U., McCarty, D.K., Derkowski, A., Fischer, T.B., Topór, T., Prasad, M., 2014b. Nano-scale texture and porosity of organic matter and clay minerals in organic-rich mudrocks. Fuel 135, 359–373. https://doi.org/10.1016/j.fuel.2014.06.036.

Lazar, O.R., Bohacs, K.M., Macquaker, J.H.S., Schieber, J., Demko, T.M., 2015. Capturing key attributes of fine-grained sedimentary rocks in outcrops, cores, and thin sections:

nomenclature and description guidelines. J. Sediment. Res. 85, 230–246. https://doi.org/10.2110/jsr.2015.11.
Loucks, R.G., Reed, R.M., Ruppel, S.C., Hammes, U., 2012. Spectrum of pore types and networks in mudrocks and a descriptive classification for matrix-related mudrock pores. AAPG Bull. 96, 1071–1098. https://doi.org/10.1306/08171111061.
Mastalerz, M., Schieber, J., 2017. Effect of ion milling on the perceived maturity of shale samples: implications for organic petrography and SEM analysis. Int. J. Coal Geol. 183, 110–119. https://doi.org/10.1016/j.coal.2017.10.010.
Mastalerz, M., Schimmelmann, A., Drobniak, A., Chen, Y., 2013. Porosity of Devonian and Mississippian New Albany Shale across a maturation gradient: insights from organic petrology, gas adsorption, and mercury intrusion. AAPG Bull. 97, 1621–1643. https://doi.org/10.1306/04011312194.
Mastalerz, M., Hampton, L., Drobniak, A., Loope, H., 2017. Significance of analytical particle size in low-pressure N_2 and CO_2 adsorption of coal and shale. Int. J. Coal Geol. 178, 122–131. https://doi.org/10.1016/j.coal.2017.05.003.
Mastalerz, M., Drobniak, A., Stankiewicz, A.B., 2018. Origin, properties, and implications of solid bitumen in source-rock reservoirs: a review. Int. J. Coal Geol. 195, 14–36. https://doi.org/10.1016/j.coal.2018.05.013.
Mazur, S., Porębski, S.J., Kędzior, A., Paszkowski, M., Podhalańska, T., Poprawa, P., 2018. Refined timing and kinematics for Baltica–Avalonia convergence based on the sedimentary record of a foreland basin. Terra. Nova 30, 8–16. https://doi.org/10.1111/ter.12302.
Mehmani, A., Prodanović, M., Javadpour, F., 2013. Multiscale, multiphysics network modeling of shale matrix gas flows. Transport Porous Media 99, 377–390. https://doi.org/10.1007/s11242-013-0191-5.
Middleton, R.S., Gupta, R., Hyman, J.D., Viswanathan, H.S., 2017. The shale gas revolution: barriers, sustainability, and emerging opportunities. Appl. Energy 199, 88–95. https://doi.org/10.1016/j.apenergy.2017.04.034.
Milliken, K.L., Olson, T., 2017. Silica diagenesis, porosity evolution, and mechanical behavior in siliceous mudstones, Mowry Shale (Cretaceous), Rocky Mountains. U.S. A. J. Sediment. Res. 87, 366–387. https://doi.org/10.2110/jsr.2017.24.
Milliken, K.L., Rudnicki, M., Awwiller, D.N., Zhang, T., 2013. Organic matter-hosted pore system, Marcellus formation (devonian), Pennsylvania. AAPG Bull. 97, 177–200. https://doi.org/10.1306/07231212048.
Milliken, K.L., McCarty, D.K., Derkowski, A., 2018. Grain assemblages and diagenesis in the tarl-dominated Lower Silurian mudrock succession of the western margin of the east European craton in Poland and Lithuania. Sediment. Geol. 374, 115–133. https://doi.org/10.1016/j.sedgeo.2018.07.011.
Modica, C.J., Lapierre, S.G., 2012. Estimation of kerogen porosity in source rocks as a function of thermal transformation: example from the Mowry Shale in the Powder River Basin of Wyoming. AAPG Bull. 96, 87–108. https://doi.org/10.1306/04111110201.
Momper, J., 1978. Oil migration limitations suggested by geological and geochemical considerations. In: Physical and Chemical Constraints on Petroleum Migration. AAPG. https://doi.org/10.1306/CE8396C2.
Nelson, P.H., 2009. Pore-throat sizes in sandstones, tight sandstones, and shales. AAPG Bull. 93, 329–340. https://doi.org/10.1306/10240808059.
Nuttal, B.C., Eble, C., Bustin, R.M., Drahovzal, J.A., 2005. - Analysis of Devonian black shales in Kentucky for potential carbon dioxide sequestration and enhanced natural gas production. In: Rubin, E.S., Keith, D.W., Gilboy, C.F., Wilson, M., Morris, T., Gale, J., Thambimuthu, K. (Eds.), Greenhouse Gas Control Technologies 7. Elsevier Science Ltd, Oxford, pp. 2225–2228. https://doi.org/10.1016/B978-008044704-9/50306-2.
Podhalańska, T., Feldman-Olszewska, A., Roszkowska-Remin, J., Janas, M., Pachytel, R., 2020. Prospective zones of unconventional hydrocarbon reservoirs in the Cambrian, Ordovician and Silurian shale formations of the East European Craton marginal zone in Poland. Geol. Q. 64, 35.
Poncet, P., 2012. Modeest: Mode Estimation. R Package Version 2, .4.0.
Poprawa, P., 2010. Potencjał występowania złóż gazu ziemnego w łupkach dolnego paleozoiku w basenie bałtyckim i lubelsko-podlaskim. Przeglad Geol. 58, 226–249.
Poprawa, P., Šliaupa, S., Stephenson, R., Lazauskien, J., 1999. Late Vendian–Early Palaeozoic tectonic evolution of the Baltic Basin: regional tectonic implications from subsidence analysis. Tectonophysics 314, 219–239.
Porębski, S., Podhalańska, T., 2019. Ordovician–silurian lithostratigraphy of the East European craton in Poland. Ann. Soc. Geol. Pol. 85, 95–104. https://doi.org/10.14241/asgp.2019.05.
Porębski, S.J., Prugar, W., Zacharski, J., 2013. Silurian shales of the East European Platform in Poland–some exploration problems. Przeglad Geol. 61, 630–638.
Preibisch, S., Saalfeld, S., Tomancak, P., 2009. Globally optimal stitching of tiled 3D microscopic image acquisitions. Bioinformatics 25, 1463–1465. https://doi.org/10.1093/bioinformatics/btp184.
R Core Team, 2020. R: A Language and Environment for Statistical Computing. R Foundation for Statistical Computing, Vienna, Austria.
Ross, D.J.K., Marc Bustin, R., 2009. The importance of shale composition and pore structure upon gas storage potential of shale gas reservoirs. Mar. Petrol. Geol. 26, 916–927. https://doi.org/10.1016/j.marpetgeo.2008.06.004.
Rouquerol, J., Avnir, D., Fairbridge, C.W., Everett, D.H., Haynes, J.M., Pernicone, N., Ramsay, J.D.F., Sing, K.S.W., Unger, K.K., 1994. Recommendations for the characterization of porous solids (Technical Report). Pure Appl. Chem. 66, 1739–1758. https://doi.org/10.1351/pac199466081739.
Rouquerol, F., Rouquerol, J., Sing, K.S.W., 1999. Adsorption by Powders and Porous Solids: Principles, Methodology, and Applications. Academic Press, San Diego.
Saidian, M., Kuila, U., Prasad, M., Barraza, S.R., Godinez, L.J., Alcantar-Lopez, L., 2016. A comparison of measurement techniques for porosity and pore size distribution in shales (mudrocks): a case study of Haynesville, eastern European silurian, niobrara, and monterey formations. In: Olson, T. (Ed.), Imaging Unconventional Reservoir Pore Systems. American Association of Petroleum Geologists, pp. 89–144. https://doi.org/10.1306/13592019M1123695.
Salama, A., Amin, M.F.E., Kumar, K., Sun, S., 2017. Flow and transport in tight and shale formations: a review. Geofluids 1–21. https://doi.org/10.1155/2017/4251209, 2017.
Schieber, J., 2016. Experimental testing of the transport-durability of shale lithics and its implications for interpreting the rock record. Sediment. Geol. 331, 162–169. https://doi.org/10.1016/j.sedgeo.2015.11.006.
Schieber, J., Southard, J.B., Schimmelmann, A., 2010. Lenticular shale fabrics resulting from intermittent erosion of water-rich muds–interpreting the rock record in the light of recent flume experiments. J. Sediment. Res. 80, 119–128. https://doi.org/10.2110/jsr.2010.005.
Schieber, J., Lazar, R., Bohacs, K., Klimentidis, R., Dumitrescu, M., Ottmann, J., 2016. An SEM study of porosity in the eagle ford shale of Texas—pore types and porosity distribution in a depositional and sequence-stratigraphic context. In: Breyer, J. (Ed.), The Eagle Ford Shale: A Renaissance in U.S. Oil Production. American Association of Petroleum Geologists, pp. 167–186. https://doi.org/10.1306/13541961M1103589.
Schindelin, J., Arganda-Carreras, I., Frise, E., Kaynig, V., Longair, M., Pietzsch, T., Preibisch, S., Rueden, C., Saalfeld, S., Schmid, B., Tinevez, J.-Y., White, D.J., Hartenstein, V., Eliceiri, K., Tomancak, P., Cardona, A., 2012. Fiji: an open-source platform for biological-image analysis. Nat. Methods 9, 676–682. https://doi.org/10.1038/nmeth.2019.
Shale gas in Poland-prospecting and exploration: 2007-2016 as of 29 February 2016, 2016. Ministry of the Environment-Department of Geology and Geological Concessions.
Sing, K.S.W., 1985. Reporting physisorption data for gas/solid systems with special reference to the determination of surface area and porosity (Recommendations 1984). Pure Appl. Chem. 57, 603–619. https://doi.org/10.1351/pac198557040603.
Środoń, J., 2001. Quantitative X-ray diffraction analysis of clay-bearing rocks from random preparations. Clay Clay Miner. 49, 514–528. https://doi.org/10.1346/CCMN.2001.0490604.
Tissot, B.P., Welte, D.H., 2013. Petroleum Formation and Occurrence. Springer Berlin, Berlin.
Topór, T., Derkowski, A., Kuila, U., Fischer, T.B., McCarty, D.K., 2016. Dual liquid porosimetry: a porosity measurement technique for oil- and gas-bearing shales. Fuel 183, 537–549. https://doi.org/10.1016/j.fuel.2016.06.102.
Topór, T., Derkowski, A., Ziemiański, P., Marynowski, L., McCarty, D.K., 2017a. Multivariable constraints of gas exploration potential in the Lower Silurian shale of the Baltic Basin (Poland). Int. J. Coal Geol. 179, 45–59. https://doi.org/10.1016/j.coal.2017.05.001.
Topór, T., Derkowski, A., Ziemiański, P., Szczurowski, J., McCarty, D.K., 2017b. The effect of organic matter maturation and porosity evolution on methane storage potential in the Baltic Basin (Poland) shale-gas reservoir. Int. J. Coal Geol. 180, 46–56. https://doi.org/10.1016/j.coal.2017.07.005.
Valenza, J.J., Drenzek, N., Marques, F., Pagels, M., Mastalerz, M., 2013. Geochemical controls on shale microstructure. Geology 41, 611–614. https://doi.org/10.1130/G33639.1.
Wang, S., 2018. Shale gas exploitation: status, problems and prospect. Nat. Gas. Ind. B 5, 60–74. https://doi.org/10.1016/j.ngib.2017.12.004.
Wang, Z., Krupnick, A., 2013. A retrospective review of shale gas development in the United States: what led to the boom? SSRN electron. J. https://doi.org/10.2139/ssrn.2286239.
Wang, R., Sang, S., Zhu, D., Liu, S., Yu, K., 2018. Pore characteristics and controlling factors of the lower cambrian hetang formation shale in northeast jiangxi, China. Energy Explor. Exploit. 36, 43–65. https://doi.org/10.1177/0144598717723814.
Wei, L., Mastalerz, M., Schimmelmann, A., Chen, Y., 2014. Influence of Soxhlet-extractable bitumen and oil on porosity in thermally maturing organic-rich shales. Int. J. Coal Geol. 132, 38–50. https://doi.org/10.1016/j.coal.2014.08.003.
Whitney, D.L., Evans, B.W., 2010. Abbreviations for names of rock-forming minerals. Am. Mineral. 95, 185–187. https://doi.org/10.2138/am.2010.3371.
Xu, M., Dehghanpour, H., 2014. Advances in understanding wettability of gas shales. Energy Fuels 28, 4362–4375. https://doi.org/10.1021/ef500428y.
Yang, F., Ning, Z., Wang, Q., Zhang, R., Krooss, B.M., 2016. Pore structure characteristics of lower Silurian shales in the southern Sichuan Basin, China: insights to pore development and gas storage mechanism. Int. J. Coal Geol. 156, 12–24. https://doi.org/10.1016/j.coal.2015.12.015.
Yang, F., Xu, S., Hao, F., Hu, B., Zhang, B., Shu, Z., Long, S., 2019. Petrophysical characteristics of shales with different lithofacies in Jiaoshiba area, Sichuan Basin, China: implications for shale gas accumulation mechanism. Mar. Petrol. Geol. 109, 394–407. https://doi.org/10.1016/j.marpetgeo.2019.06.028.
Yang, F., Zheng, H., Lyu, B., Wang, F., Guo, Q., Xu, H., 2021. Experimental investigation about gas transport in tight shales: an improved relationship between gas slippage and petrophysical properties. Energy Fuels 35, 3937–3950. https://doi.org/10.1021/acs.energyfuels.0c04086.
Yu, H., Zhu, Y., Jin, X., Liu, H., Wu, H., 2019. Multiscale simulations of shale gas transport in micro/nano-porous shale matrix considering pore structure influence. J. Nat. Gas Sci. Eng. 64, 28–40. https://doi.org/10.1016/j.jngse.2019.01.016.
Zhu, X., Cai, J., Liu, Q., Li, Z., Zhang, X., 2019. Thresholds of petroleum content and pore diameter for petroleum mobility in shale. AAPG Bull. 103, 605–617. https://doi.org/10.1306/0816181617517009.